In vivo Partial Reprogramming by Bacteria Promotes Adult Liver Organ Growth without Fibrosis and Tumorigenesis

In vivo Partial Reprogramming by Bacteria Promotes Adult Liver Organ Growth without Fibrosis and Tumorigenesis

Samuel Hess[1, 2 †], Timothy J. Kendall [1, 3, 4 †], Maria Pena[5 †], Keitaro Yamane[1, 2], Daniel Soong[1, 6], Linda Adams[5], Richard Truman[5, 7], Anura Rambukkana[1, 2, 8, 9, 10 *]

[1] Institute for Regeneration and Repair, The University of Edinburgh, Edinburgh, UK

[2] Centre for Regenerative Medicine, The University of Edinburgh, Edinburgh, UK

[3] Centre for Inflammation Research, The University of Edinburgh, Edinburgh, UK

[4] Edinburgh Pathology, The University of Edinburgh, Edinburgh, UK

[5] United States Department of Health and Human Services, Health Resources and Services Administration, Healthcare Systems Bureau, National Hansen's Disease Program, Baton Rouge, LA, USA

[6] Medical Research Council Centre for Reproductive Health, The University of Edinburgh, Edinburgh, UK

[7] Department of Pathobiological Sciences, School of Veterinary Medicine, Louisiana State University, Baton Rouge, LA, USA

[8] Edinburgh Infectious Diseases, The University of Edinburgh, Edinburgh, UK

[9] Centre for Discovery Brain Sciences, The University of Edinburgh, Edinburgh, UK

[10] Lead contact

[†]These authors contributed equally

[*] Correspondence: a.rambuka@ed.ac.uk

Short title:

Functional *in vivo* organ growth in living animals with bacteria

Key words:

Organ growth, Liver regeneration, Partial Reprogramming, Rejuvenation, Aging, Machine learning, Stem cells, Regenerative Medicine, *Mycobacterium leprae*, Nine-banded armadillo

SUMMARY

Ideal therapies for regenerative medicine or healthy aging require healthy organ growth and rejuvenation but no organ level approach is currently available. Using *Mycobacterium leprae* (ML) with natural partial cellular reprogramming capacity and its animal host nine-banded armadillos, we present an evolutionarily refined model of adult liver growth and regeneration. In infected-armadillos, ML reprogram the entire liver and significantly increase total liver: body weight by increasing healthy liver lobules including hepatocyte proliferation and proportionate expansion of vasculature, and biliary systems. ML-infected livers are microarchitecturally and functionally normal without damage, fibrosis or tumorigenesis. Bacterial-induced reprogramming reactivates liver progenitor/developmental/fetal genes, and upregulates growth-, metabolism-, and anti-aging-associated markers with minimal change in senescence and tumorigenic genes, suggesting bacterial hijacking of homeostatic, regeneration pathways to promote de novo organogenesis. This may facilitate the unravelling endogenous pathways that effectively and safely re-engage liver organ growth, with broad therapeutic implications including organ regeneration and rejuvenation.

INTRODUCTION

Adult organ growth promotion or rejuvenation are idealized strategies for treating dysfunction in disease, injury, or aging[1–3]. Such strategies must engage highly coordinated multilineage functions *in vivo.* Although *in vitro* models, organoids, and mini-organs have potential for drug discovery, disease modeling and regenerative medicine[4,5], they fail to model required organ-level complexity. Consequently, despite advances in such approaches[2,5], no current strategy achieves effective regrowth or rejuvenation of adult organs in chronic or aging-associated human diseases

Liver is the exemplar organ for studying growth and regeneration[6,7]. Unlike other solid organs, adult liver has capacity to regain the prior mass after tissue loss, restoring homeostasis[7]. In human chronic liver disease, repeated inflammatory injury and parenchymal cell death stimulate regenerative restitution of the liver cell mass in parallel with a wound healing response[8]. Some regenerative capacity remains in cirrhosis although complete recovery is impossible and transplantation remains the only treatment. Chronic injuries are associated with increased risk of malignancy, highest in chronic viral infections[9,10]. Endogenous pathways regenerating damaged liver remain poorly characterized and failures of understanding contribute to a lack of pro-regenerative clinical strategies. As the health and economic burden of liver diseases rapidly increases[11,12], the absence of such repair strategies is critical. Moreover, the aging liver is more prone to progressive diseases as physiological functions decline[13–15]. Maintenance of healthy liver for healthy aging is critical as it directly or indirectly influences other organ function but there are no rejuvenating strategies slowing or reversing declining liver function during aging.

Current study of liver regeneration uses short-lived rodent models requiring hepatocyte loss to stimulate regeneration[8,16,17] that ceases when the original liver size is reached. Mechanisms stopping the response once the prior organ size is reached are unknown[17]. The ability to by-pass such upper-limit restriction would allow regeneration to be studied without prior liver injury. Understanding how regenerative machinery can be engaged de novo will provide paradigm-shifting adult organ regrowth and rejuvenation clinical strategies that could reduce or replace transplantation but no such *in vivo* model is currently available.

Recent studies using the overexpression of the OSKM factors (Oct4, Sox2, Klf4, c-Myc)) that originally generated induced pluripotent stem (iPS) cells from somatic cells [18–23] showed a proof-of-principle that resetting committed cells to a progenitor stage of the same lineage permits tissue regeneration and rejuvenation. Therefore, alternative approaches that potentially increase adult tissue plasticity, proliferation, and de-differentiation should also be explored as strategies for tissue rejuvenation and regeneration.

Our studies on the biology of *Mycobacterium leprae* (ML)-host interaction [25–28] led to the identification of ML's natural ability to hijack the plasticity and regenerative properties of adult Schwann cells, partially reprograming them into a progenitor cell/stem cell state beneficial to the bacteria[29]. At the host level, ML-induced reprograming promotes growth of infected tissues permitting bacterial propagation[25,26,29,30]. These host-dependent features of ML without cytopathic or adverse effects during the establishment phase of infection permit use of ML as an evolutionary adapted bacterial model for dissecting undefined host endogenous pathways [30,33,34, 35,36].

Nine-banded armadillos (*Dasypus novemcinctus*) are New World placental mammals, the only mammal to produce four genetically identical/clonal litters, and a natural host of ML[36–38]. Experimental inoculation with viable ML produce disseminated infection [36–40] , and their lifespan (12-13 year in the wild, up to 20 years in captivity) and core body temperature (32-35°C) are optimal for *in vivo* ML replication[36–38]. Since their discovery as a natural host of ML[38], armadillos have been used for *in vivo* propagation of ML in the liver for harvesting bacteria for research[39]. We explored if this co-evolved bacterial pathogen in the liver of susceptible hosts exploited the same reprogramming strategies to expand host cells *in vivo* during natural infection as those observed *in vitro* in adult Schwann cells[29].

We report a natural *in vivo* model of ML infected nine-banded armadillos for mammalian adult liver growth at organ level without prior injury. We showed that bacterial-induced *in vivo* partial reprogramming significantly increased liver size with sustained function and architecture but without damage, fibrosis or tumorigenesis during the establishment phase of infection. We define which cell types promote this organ growth and show that healthy liver lobule number, not size, with a proportionate expansion of the hepatocyte mass and vascular and bile ductal systems, are responsible. We delineate the molecular details to show evidence that ML have adapted dynamic partial reprogramming, regenerative, and developmental/fetal mechanisms to promote de novo liver organogenesis while maintaining tissue-protective and tumor preventive strategies.

RESULTS

In vivo ML infection of nine-banded armadillos promotes organ growth

Adult nine-banded armadillo (>1.5 to 2 years old) livers with disseminated infection ('infected') after injection of viable ML were compared with those from animals resistant to infection ('resistant') and uninfected animals (Fig. 1; Suppl Fig.1, Suppl Table 1; Methods). During natural infection, ~95% of humans and 20% of armadillos clear ML immediately while infection progresses in the remainder. Clonal armadillo siblings (Fig.1A) were either fully resistant to infection or showed disseminated infection, indicating a strong heritable component for susceptibility and clearance. Resistant animals showed

initial responses to infection, determined by serum ML-specific phenolic glycolipid-1 (PGL-1) antibody levels (Suppl Fig. 1C; Methods), but bacteria failed to propagate in the liver and only a few, presumably non-viable or dead, bacilli remained (Fig. 1G; Suppl Table 1). Total liver:body weight was significantly increased in armadillos infected for a period of 10-30 months compared to resistant ($p < 0.0018$) or uninfected animals (<0.001) (Figs. 1B, D, F). Livers from most infected animals showed a high bacterial count (up to 3.0E11 bacilli/g) (Figs. 1C, F, G, Suppl Fig.1; Suppl Table 1). Liver:body weight correlated with hepatic bacterial load in infected animals ($rs = 0.5775764$, $p = 0.00007687$, Fig. 1E). Immunolabeling with an ML-specific anti-PGL-1 antibody and Wade-Fite acid-fast mycobacterial staining[29,32] revealed ML in most hepatocytes and macrophages in small granulomas in infected animals (Fig.1C; Suppl Fig 1D).

Armadillos comprised clonal animals, and wild-born or captive-born animals (Fig. 1A; Suppl Table 1). Clonal infected animals showed almost identical liver mass increases and bacterial counts (Suppl Fig.1) but there was no difference in these metrics between wild- or captive-born animals, or between males and females (Suppl Table 1). The influence of non-ML infection was excluded by clearance of prior infection with antibiotic, antifungal and antiparasitic drug treatment for >1 year in captivity prior to inoculation. Identical treatment of resistant and uninfected animals did not induce liver growth. Therefore, we concluded that ML-induced liver growth is unique and specific.

Enlarged infected livers have intact architecture and vascular organization without damage, fibrosis, steatosis or tumor formation

In vivo ultrasonographic assessment demonstrated identical liver echotexture and normal lobation in all groups; livers of infected animals were enlarged (Figs. 1B). Macroscopic examination confirmed identical lobation in all groups, with smooth, uniform capsules (Figs. 1D; Suppl Fig 1A, B). Livers from infected animals were larger but all lobes were enlarged similarly, and their relative proportions normal (Figs 1D; Suppl Fig 1A, B). On sectioning, the parenchyma of livers from each group was identical. No masses were present in livers of any animal. (Figs 1D; Suppl Fig 1A, B).

ML were demonstrable in the cytoplasm of cells with characteristic hepatocellular nuclear features and distribution (Fig. 1C; Suppl Fig 1D). Blinded histological examination of random parenchymal blocks revealed that the portal-central vascular relationships of normal mammalian liver were present in the livers of infected animals (Figs. 2A, 3E, 4C, E, Suppl Fig. 2). Hepatocytes were present in single cell plates, separated by sinusoidal vascular channels (Figs. 1H, I, 2A-G; Suppl Fig. 4). Infected livers showed variable inflammation and irregularly distributed small non-necrotizing granulomas consisting mostly of bacteria-laden macrophages (Suppl Figs 1-c, 10). Focal, pericentral cell-plate twinning was present in a single infected animal, suggesting regenerative activity (Suppl Fig. 5).

There was no other abnormality in infected livers (Figs. 1H, 4C, E; Suppl Figs 1, 2, 5). Specifically, no hepatocellular ballooning, steatosis, or cell death (apoptotic acidophil bodies, necroinflammatory foci, or TUNEL positive cells), nor evidence of prior cell death ('ceroid-laden' macrophages). There was no portal or parenchymal edema, no sinusoidal dilation, and no nodularity. There was no dysplasia in the livers of any animal (Figs.1H, 4C, E B;). There was no scarring demonstrable on sensitive extracellular matrix stains (Figs. 1I, 4, B). The inflammatory injury, steatosis, and scarring seen in chronic human inflammatory diseases due to chronic viral infection, autoimmune injury, or metabolic injury (Fig 4F) were not present in infected armadillo livers. Serum levels of the liver functional enzymes aspartate transaminase (AST), alanine transaminase (ALT) and lactate dehydrogenase (LDH) were not deranged in infected animals during the early stage of bacterial propagation while serum antibody responses to ML remained high, indicating the absence of hepatocellular injury during infection-induced liver growth (Fig. 1J).

Architectural integrity of infected enlarged livers: To quantitatively evaluate the architectural integrity of infected liver, positions of portal tracts and central veins were annotated on images of H&E-stained sections (examples from 10 animals in each group are shown in Suppl Fig 2) and spatial point patterns created (Fig. 2A). The distribution of all annotated vascular structures was quantified and groupwise analysis demonstrated no differences (studentized permutation test for grouped point patterns, Tbar (999 random permutations) = 1.6353, p-value = 0.549); in all groups, large vascular structures were evenly dispersed (empirical function plots below the yellow line that represents complete spatial randomness), and there was no loss of the regular arrangement in the disseminated animals (Fig. 2B). To understand the fractal geometry of the biliary tree in the enlarged livers, the intensity of portal tracts in the 2-D sections was calculated. The portal density in the livers of animals with disseminated infection was significantly different by one-way ANOVA ($F(2,41) = 4.115$, $p = 0.0235$); post hoc comparison using the Tukey HSD test indicated that the mean density in infected animals was less than that of the control animals ($p = 0.01999$) suggesting elongation of the individual branches in addition to any branching occurring during liver growth (Fig. 2D).

Proportionate lobular expansion in infected enlarged livers: To model the cross-sectional representation of functional lobular units of the liver, nearest-neighbor distances between portal tracts and central veins were calculated to allow lobule area to be determined, based on the hexagonal paradigm often used to represent the polygonal lobules with between 3 and 7 faces in mammals[41]. Polygonal liver lobules most commonly have portal tracts at three apices although this, too, is variable. To determine if this assumption could be used to calculate a mean value for the radius of each lobule, the nearest six portal tract neighbors to each separate central vein profile in control animals were calculated (Fig. 2C). The greatest difference between the mean of the k and k+1 neighbors was at the k=3:4 boundary, indicating that the nearest three portal tracts were segregated from the next nearest

179 portal tracts in armadillo liver and the mean of these values for each central vein was used to calculate
180 modelled lobule size. The size of individual lobules was not significantly different between groups by
181 one-way ANOVA ($F(2,41) = 2.702$, $p = 0.079$, Fig. 2E). These findings collectively indicate no
182 microscopic abnormality in infected livers despite long-term ML infection and organ enlargement,
183 suggesting ML-induced liver organ growth involves proportionate vascular, biliary and lobular growth.

184

185 ## Increased hepatocyte mass in ML-induced liver growth

186 To assess which liver cell type(s) contribute to ML-induced liver growth, we quantified the cellular
187 composition of liver sections using machine learning cell classification (Fig 2F, Methods, Suppl Table
188 2). All cells in DAPI-stained liver sections were classified based on nuclear morphology as 'classical
189 hepatocytes' with large spherical nuclei (Figs 2G, H), 'binucleated hepatocytes' (Figs. 2H, I), or non-
190 hepatocytes ('other') using a manually-trained machine-learning classifier (Figs 2H-J; Suppl Figs 2, 3,
191 4). While some errors are apparent in these representative regions, they are in the expected range
192 (Suppl Table 2) considered valid for analysis across whole sections. Accuracy of classification is
193 supported by the localization of hepatocytes (in yellow) within hepatocyte plates (Fig. 2H, Suppl Figs 3,
194 4, 8E), and the localization of purple-labelled 'non-hepatocytes/other cells' within vessel walls,
195 granulomas, and sinusoids (Suppl Figs. 3, 4, 8E).

196 Confirmation was provided by labelling with a cross-species (mouse/human) antibody for the
197 hepatocyte-specific transcription factor (TF) HNF4α (Fig 2K, Suppl Fig 8E). This demonstrated that
198 nuclear HNF4α immunopositivity correlated with classified single (Figs. 2H-K) or binucleated
199 hepatocytes (Figs. 2K-b); there was no HNF4α immunopositivity in nuclei of cells classified as 'non-
200 hepatocytes/other' (Figs. 2K-a; Suppl Fig. 8E). The normal sinusoidal architecture in livers of animals
201 with disseminated infection was visible from the normal hepatic autofluorescence (Figs. 2I, Suppl Fig.
202 4).

203 Using this classification, the density of nuclei of each cell class was calculated. The mean density of
204 classical hepatocytes in each group was not significantly different by one-way ANOVA ($F(2,26) = 0.185$,
205 $p = 0.832$, Fig. 2K). There were more binucleate hepatocytes in infected livers compared with controls
206 although the mean number for each group did not differ significantly by one-way ANOVA ($F(2,26) =$
207 3.112, $p = 0.0614$). There were also more 'other' cells in infected livers of infected animals, reflecting
208 variable inflammation and focal small granulomas; whilst the mean number was significantly different by
209 one-way ANOVA ($F(2,26) = 4.653$, $p = 0.0187$), there was no significant difference between the mean
210 number of 'other' cells in control and infected animals by post-hoc Tukey HSD testing ($p = 0.1349992$),
211 (Fig. 2K), suggesting that 'other' cells, which mostly comprise immune and endothelial cells, are not
212 responsible for the increased parenchymal mass in infected livers. These combined analyses show that

the microarchitectural lobular organization and hepatocellular composition of infected enlarged livers were normal, in keeping with the macroscopic and histopathological normality (Fig. 2, Suppl Fig. 4). The enlarged liver in disseminated ML infection is not a consequence of pathological 'inflation' of lobules, which would be associated with a decrease in hepatocellular density, but shows lobules of normal size and with normal hepatocyte density, indicating 'normal' organ growth and proportionate expansion of vascular and ductal systems promoted by ML (Figs. 2L, M, N).

RNA-sequencing of ML-infected livers with human gene annotation reveals large transcriptional changes reflecting partial hepatocellular reprogramming

RNA-sequencing (RNAseq) was undertaken to define the molecular signature underlying ML-induced liver growth. Among protein-coding genes, 99.5% of those with gene symbols are shared with annotated human genes so known mammalian gene functions were used to interpret armadillo RNAseq data (Figs. 3A-C; Methods). Gene ontology (GO) analysis of differentially upregulated genes in infected livers demonstrate upregulation of cellular activation, progenitor markers and metabolic processes that conceptually connect to increased liver cell mass (Figs 3, 4). Enrichment of 'Regeneration', 'Homeostatic process' and 'Wound healing' further suggests that the liver growth could involve endogenous regeneration, homeostasis and repair pathways (Figs. 3C, D, 6A, B). Enrichment of genes associated with GO terms for vascular development, angiogenesis, and bile duct formation-related processes, and upregulation of numerous ECM and collagen genes, are in keeping with expansion of vascular and biliary systems and the generation of supportive matrix for these newly formed vascular and ductal structures (Figs. 3C, D, Suppl Fig. 4). Selected genes related to liver development, growth, cell cycle progression and regeneration (based on mouse and human studies) are shown in Fig 3D.

All normal liver cell types contribute to the growth of infected armadillo livers based on predicted similarities to human liver single cell transcriptomes

To investigate the contribution of different cell types, based on their gene expression, to ML-induced liver growth further, we cross-referenced differentially expressed armadillo genes with human liver single-cell (sc) RNAseq data[42]. ML-induced genes are associated with all key liver cell types in armadillos (Figs 3H-L, Data S1), in keeping with proportional functional contribution to liver growth at the organ level.

ML-infected enlarged livers are pro-regenerative but non-fibrogenic

Next, we compared transcriptional features of ML-infected armadillo liver to rodent fibrotic and regenerative models, human liver diseases, and human fetal liver. In adult livers, upregulation of ECM markers is associated with fibrosis[8,43]. When compared to our previously described mouse model of

fibrosis[43], we found that the transcriptional response in infected liver overlaps with that seen after activation of quiescent hepatic stellate cells into myofibroblasts responsible for ECM production and organization, a shared effector event in fibrotic liver disease[43] (Supl Figs. 7B, C). However, the number of genes coding for different collagen species upregulated, and the extent of upregulation, is muted in the unscarred livers of ML-infected animals compared with the profibrotic response to injury in the mouse fibrosis model (Fig 4A, B), in keeping with the absence of histological fibrosis (Figs. 1H, 1I, 4C).

To further support the hypothesis that ML infection induces a liver progenitor-like state *in vivo* and demonstrate potential relevance of our findings to human liver regeneration, we compared the transcriptome of infected armadillo livers with adult and fetal hepatic progenitors or related populations defined from single cell scRNAseq analysis of human liver[42,44,45]. Despite the difference in species, technology and biological context, a signal attributable to hepatocyte progenitors was clear. A range of fetal and adult liver progenitor-like markers are upregulated in the livers of infected armadillo livers, suggesting *in vivo* generation of progenitor populations. Livers of infected armadillos show upregulation of genes whose expression defines populations of fetal (fHep) and adult hepatocytes, fetal (fHHyP)_and adult hepatobiliary hybrid progenitors, and adult biliary epithelial cells in human liver (Fig 4G)[45], including the fetal hepatocyte marker AFP and the progenitor markers PROM1 and FGFR2. The shared genes upregulated in infected armadillo livers and those defining fHHyP and fHep map to GO terms such as wound healing responses and metabolic processes.

Importantly, there is also upregulation in infected armadillo livers of 477 markers of EPCAM1+ progenitor populations in adult human liver defined by Aizarani et al[42] (including PROM1, SFRP5, CLDN3, CLDN4, CLDN10 and ANXA4), markers of a central population of uncommitted bipotential epithelial progenitor cells (SFRP5, FGFR2), and markers defining both hepatocyte-biased (ALB, SERPINF1, and FGB) and cholangiocyte-biased progenitors (ANXA2, BIRC3, and TM4SF1). The GO terms significantly mapped to the shared genes upregulated in ML-infected armadillo liver and defining the EPCAM+ progenitor cluster from normal adult human liver (cluster 4) are shown in figure 4H and the full g:profiler report is provided in Data S2.

Furthermore, MacParland et al[44] determined differential gene expression in AFP-positive versus AFP-negative cells, proposing that AFP-positive cells throughout lobules in adult liver represent a heterogenous population of hepatic progenitor cells; there were 233 shared genes upregulated in AFP-positive versus AFP-negative cells and in infected armadillo livers, and the GO term mapping of these included miRNA and organonitrogen metabolic processes. 144 shared genes were downregulated in the same comparisons, mapping to RNA biosynthetic and metabolic processes, and chromatin organization. The complete gProfiler reports of GO term mappings using the sets of shared up or down-regulated genes are shown in Data S2.

ML reactivates liver regeneration-associated genes similar to rat hepatectomy model: In a rat partial hepatectomy model, a model of rapid liver regeneration[46], there were 60 upregulated genes also upregulated in ML-infected armadillo livers. These shared upregulated genes map to GO terms related to cell division and subcellular organization (Fig. 4H). Only 17 genes were equivalently down-regulated in both model systems.

ML-infection selectively induces trophic factors/pathways while preserving liver functional markers

Expression of specific known liver trophic factors were examined (Figs. 3D, 5). FOXA TFs are regulators of embryonic hepatic specification and development, as well as adult biliary function[47,48] and parenchymal homeostasis[49]. The transcriptome from infected animals showed significant upregulation of FOXA1, FOXA2 and FOXA3 (Figs. 3D, 5A). We also found that LGR4 and LGR5, promotors of Wnt/β-catenin signaling in development[50] and involved in control of liver size, growth and zonation[5,51], are upregulated in ML infection. Further, hepatocyte growth factor (HGF), a potent hepatic mitogen[52], and insulin-like growth factors-1 and -2, major niche factors for tissue survival, proliferation and growth expressed in regenerating livers and important stimulant for both mouse and human liver organoid expansion[5,53,54], are also induced (Fig. 3D, Suppl Fig 9). In addition, there is induction of other well-described growth factors and their receptors and binding proteins involved in development and regeneration, including BMP1, BMP5, BMP10, TGFB, FGFR4, IGF2R, IGFBP7[6,8,9,16] (Fig. 3D; Suppl Fig 9).

To confirm transcriptional data at the protein level, we used available cross-reactive antibodies (Figs. 5B-G; Suppl Methods). We found increased protein expression of developmental or homeodomain transcription factors FOXA1/2, HNF4α, SOX9, SOX17, GATA6, adhesion molecules E-Cadherin and ß-Catenin, and trophic factors such as IGF family proteins (Figs 5B, E, F, G; Suppl Figs. 4, 8). Liver functional proteins albumin, HNF4α, AFP, CEBP/α and CYP members are expressed or upregulated at protein levels from whole liver extracts and individual cells in situ from infected animals (Figs 5B, E, F, G).

The distribution of hepatocytes expressing FOXA1/2 and HNF4α was examined in detail. HNF4α is upregulated in infected livers and specifically expressed in hepatocytes (Suppl Fig 8). Hepatocytes with nuclear FOXA1/2 immunopositivity were pericentral and midzonal but absent from portal and periportal areas (Figs. 5B); neither were detectable in uninfected armadillo and normal human liver (Figs 5C, D). However, the pattern of expression of other functional liver markers in infected armadillo livers (albumin, E-Catherin, HNF4α, ß-Catenin, and CD68) was similar to normal human liver (Figs 5G, H), suggesting

ML-infected livers share common molecular and histopathological features with normal human adult livers.

The Hippo pathway is associated with liver growth, regeneration, and cancer development[55]. Only a few pathway members were differentially modulated in infected livers at gene and protein level. Moreover, the activation of member proteins by phosphorylation, critical for downstream regulation of liver growth[17,55] was absent (Suppl Fig 9). Of detectable YAP/Taz target genes, the majority showed no significant difference and only a few showed marginally increased expression in infected animals (Suppl Fig 9D).

ML influence anti-aging-associated gene patterns in armadillo liver

The comparison of transcriptomes of infected adult armadillo liver with human fetal liver revealed an inverse relationship with aging-associated genes (Fig. 6A, B). Genes mapped to the GO term 'aging' (specifically IGFBP5, IGFBP1, IGFBP2) were downregulated both in AFP-positive human progenitor-like hepatocytes and ML-infected armadillo livers whereas known anti-aging markers such as RGN/senescence Marker Protein-30, which suppresses oxidative stress in the liver and is downregulated during aging[56], was significantly upregulated both in infected livers and in human fetal livers (Figs 4D, 6A). In addition, since senescence is directly associated with aging[57], we also examined senescence-related genes[58] in infected livers. There was only minimal differential expression of known senescence inducer or inhibitor genes in infected animals, without change in master regulators of senescence such as p21, p16 and p57. Since senescence is a hallmark of aging, the absence of induction of senescence programs in infected livers aligns with potential bacterial halting of natural aging process (Fig 6C).

Other liver growth-associated genes map to GO terms including 'regeneration', 'developmental maturation', 'wound healing', 'homeostatic processes', 'response to growth factors' and 'epithelial cell proliferation' (Figs 6A, D, E). Importantly, in keeping with our previous demonstration that ML induces proliferation of rodent and human adult Schwann cells using ERK1/2 signaling pathways[26,28], we mapped ML-induced genes to the GO term 'ERK1 and ERK2 cascade' in infected livers (Fig. 6E), suggesting a potential common signaling mechanism used by ML for survival, proliferation, and de-differentiation of both Schwann cells and hepatocytes.

Bacterial-induced hepatocyte proliferation contributes to liver growth

At the transcriptional level, infected armadillos significantly upregulated 8 species of cyclins (cyclin A, D, E, G, I, J, and Y) and their cyclin dependent kinases, and also downregulated many cell cycle-

associated genes, suggesting that ML exert a dynamic regulation of cell cycle to balance liver cell proliferation and redifferentiation (Figs. 3D, 4H, I, 6A, D, E). The proliferation marker PCNA was upregulated at transcript level in ML-infected liver (Fig. 6F) and there were significantly increased PCNA immunopositive hepatocytes in infected livers (Fig 6F, G, H). Increased binucleated cells and E-cadherin in infected livers may also indicate a regenerative-like hepatocyte phenotype created during ML infection (Fig 6I). Also, in agreement with our previous findings of ML's capacity to induce proliferation of Schwann cells using ERK1/2 signaling pathways[26,28], we also mapped ML-induced genes to the GO term 'ERK1 and ERK2 cascade' in infected livers (Fig. 6E), suggesting a potential common signaling mechanism used by ML. Together, these results provide evidence for the contribution of hepatocyte proliferation to bacterial-induced organ growth.

Although we did not find a significant increase of the non-hepatocyte ('other') cell population that includes immune cells in infected livers (Fig. 2), we analyzed the potential involvement of macrophages as they are known to be associated with liver regeneration and disease[16,17]. We generated and characterized antibodies specific for nine-banded armadillo macrophages using an amino acid sequence of armadillo CD68 (Figs 5E; Suppl Fig 10; Methods). Although anti-CD68 antibodies detect a macrophage population in both control and infected armadillo livers, there was no significant increase in CD68 protein in the total liver lysates or in situ CD68+ cells in infected livers (Figs 5E, G).

Infected enlarged livers show normal zonation and functional metabolic markers

Infected livers express albumin, BAAT (involved in bile acid synthesis), CYP gene family members, and other liver metabolic genes required for normal liver functions (Figs 5A-C, 6J; Suppl Fig 6). In infected livers, the hepatocellular metabolic functions including glucose, protein, drug/steroid, and bile acid metabolic processes are upregulated (Suppl Fig 6). *In situ* analysis of liver zonation using mature hepatocyte functional markers (GS, CPS1, Cyp3A4 and Cyp2D6) showed that infected livers not only maintain the pattern of zonation present in uninfected armadillo livers but also demonstrate functional maturity similar to that of normal human liver (Figs 5F-G, 6J, K).

Mycobacterial pathogens require host cell provision of lipid for survival, lipid-rich cell wall synthesis, and replication[31]. In the transcriptome of infected livers, genes mapping to lipid metabolism are greatly upregulated (Suppl Fig. 6) but no lipid accumulation is evident with a specific lipid staining (Suppl Figs. 6C, D), suggesting bacterial lipid utilization prevents visible accumulation. The liver is at high risk for cancer development when chronic infection and inflammation are sustained[60]. However, we found no histopathological evidence of dysplasia or neoplasia in infected livers (Figs. 1, 4). To understand this further, we examined known oncogene and tumor suppressor gene expression and found only minimal

differential expression of these in infected animals, corroborating the histological evidence for the lack of tumorigenesis (Suppl Fig. 7).

DISCUSSION

Strategies promoting organ growth without abnormality are the goal of regenerative medicine or for rejuvenation during aging. Using an evolutionarily refined *in vivo* bacterial model – *M. leprae* and its natural animal host, the nine-banded armadillo – we present a model of adult liver growth without adverse effects during the establishment phase of infection. Our natural model may facilitate the unravelling of *in vivo* endogenous pathways that effectively re-engage liver growth, with potential therapeutic implications for safer liver regeneration and rejuvenation.

Liver disease accounts for 2 million deaths/year[11]. Although a prime candidate for regenerative therapies, no trial using laboratory-grown stem cells for the treatment of cirrhosis has yielded any licensed therapy[61]. The failure to develop therapies for solid organ disease using injected stem cells suggests that alternative strategies reflecting organ growth and regeneration complexity should be explored. 2-D, 3-D, and *in vitro* models have shown advances but their clinical application to large solid organs is limited[2,5]. Moreover, current knowledge of *in vivo* liver regeneration is derived from short-lived rodent injury or hepatectomy models[8,16,52].

Injury or hepatectomy-induced growth ceases when the original liver size is reached but the mechanism stopping the regenerative response is unknown. The ability to by-pass such upper-limit restriction would allow mechanisms of regeneration to be studied without prior injury or cell loss. Our findings show that ML engage endogenous regenerative liver pathways, stimulating organ growth *in vivo* while maintaining intact architecture, vascular systems and functionality. Although unexpected and unconventional, this evolutionary refined *in vivo* model may advance our understanding of the native regenerative machinery and determine how it can be engaged de novo to permit new organ regrowth strategies for potential clinical use, a conceptual advancement with broader implications in regenerative medicine.

Considering the strictly host-dependent intracellular lifestyle and limited protein-encoding genes[31], it is not surprising that ML have evolved sophisticated strategies inducing host cell proliferation, regeneration, and growth[30, 33, 35, 67, 68] . ML may also take advantage of regenerative and metabolic properties of livers. The metabolically rich liver microenvironment compensates for known ML metabolic defects, inducing numerous metabolic genes in infected livers. Since the observed *in vivo* healthy liver growth is not stimulated by other bacterial species or drug treatment, liver growth appears to be ML-specific. Maintenance of an expanded functional liver permits host cell-dependent intracellular bacterial propagation during the establishment phase of infection. Given the variable presence of immune cells

but absence of histological cell death or fibrosis, one can speculate that part of the adaptation of the host response by ML involves modulation of innate immune cell activity, preventing tissue damage.

We have previously shown that ML hijack the plasticity and regenerative properties of adult Schwann cells by partially reprogramming them into a neural progenitor/stem cell-like state permitting bacterial propagation and dissemination[29 30,33,35]. Indeed, we showed ML also promote proliferation of adult human Schwann cells[26,28], a finding replicated *in vivo* in sensory neuron-associated armadillo Schwann cells[62]. Translating this bacterial-induced partial reprogramming to *in vivo* liver organ growth, our data suggests that ML utilizes a similar evolutionary-refined strategy in adult liver by *in vivo* partial reprograming hepatocytes into liver progenitor-like cells leading to proliferation and subsequent re-differentiation upon exposure to niche factors generated within the bacterially-created, tissue regeneration-favorable microenvironment (Fig 7). Indeed, numerous tissue-specific progenitor markers were reactivated or upregulated in infected livers. Heterogeneous *in situ* expression of FoxA1/2 , not detectable in uninfected livers, was readily identified in midzonal hepatocytes recently identified as the main source of hepatocellular replenishment in liver homeostasis[63,64]. The cyclical, dynamic generation of progenitor and mature/differentiated hepatocyte populations and released trophins potentially leads to this growth (Fig 7). Additional studies are needed to compare the effects of ML infection with more conventional liver injury-repair approach in armadillos, particularly to identify molecular pathways that discriminate the hepatic response to injury vs ML.

Recent progress in cellular reprogramming has re-visited the potential of OSKM factors in tissue rejuvenation[19–22]. In mice, liver-specific expression of OSKM enhanced regeneration by partial reprogramming[19]. Since long-term overexpression of OSKM *in vivo* leads to the development of totipotent cancers in mice[24], the safety of partial reprogramming using OSKM that are expressed and activated in many human cancers[65,66], in tissue repair or growth must be clarified before clinical consideration. In contrast, in bacterial model with natural partial liver cell reprogramming, bacteria have evolved protective mechanisms to avoid these adverse effects. Understanding these mechanisms may inform new rejuvenating interventions both for liver and other adult aging organs. Indeed, the findings that ML also downregulate genes associated with aging and upregulate genes involved in anti-aging process without activating senescence suggest that ML may have evolved to rejuvenate the adult liver, maintaining a 'youthful' state with active metabolism favoring host function-dependent bacterial survival and replication for an extended period. This evolutionary refined bacterial strategy may also occur in other ML-infected highly regenerative adult tissues particularly skin and peripheral nerves. Our previous studies have shown partial reprogramming of adult Schwann cells by ML converts infected cells to a 'youthful' progenitor/stem cell stage and, on this basis others have predicted that ML could 'turn back the clock' in host cells[67,68].

Importantly, in our model the entire infected liver grows larger with new tissues in vivo, without injury, senescence, fibrosis or tumor formation but with normal architecture and function, demonstrating that adult livers can grow *in vivo* without injury or cell loss and thus regenerative medicine's pursuit of a 'grown-to-order' functional organ is not theoretical but has a naturally occurring precedent. Most critically, understanding how the regenerative machinery can be engaged de novo in a long-lived larger mammalian model will potentially allow the development of new and safer organ regrowth strategies for clinical use that could reduce or replace the need for transplantation or rejuvenating aging livers that could facilitate healthy aging.

LIMITATION OF STUDY

Our studies are limited by lack of available molecular tools, as the nine-banded armadillo is not a commonly used organism. Considering the much of the known biology comes from short-lived rodent models and their limitations for chronic and aging-associated human diseases, and the value of the long-lived and large mammalian models to gain fundamental biologies[92] it is worth developing new reagents specific for them. Eventual pathogenic events of late infection have not been addressed. ML cannot be genetically manipulated but the bacterial genome is a valuable resource for future studies. Future advances that overcome such obstacles could pave the way for our understanding of mechanistic detail as to how ML promote new liver tissue generation and drive liver growth. To further delineate liver rejuvenation *in vivo*, aging trajectories and mature cell identity need to be analyzed simultaneously with parameters of known cellular aging hallmarks, although the endpoint of this natural bacterial approach has already produced 'youthful' liver tissues at organ level without adverse effects, which is a safer outcome one would expect from any experimental regenerative and rejuvenating interventions.

ACKNOWLEDGEMENTS

We acknowledge Roena Stevenson, Judith Wiles, Rachel Walley, and Gregory McCormick for animal studies, and Lyndsey Boswell, Melanie McMillan, and Michael Millar (SuRF@Little France) for histology and imaging. We thank Yanggu Shi and the bioinformatics team at (Arraystar Rockville, MD), Jaminson McCorrison and John Glass (J Craig Venter Institute, CA), and Rahul Sharma (NHDP) for sequencing assistance, and David Hay and Luke Boulter (UoE) for antibodies. We acknowledge Julia Martina-Rambukkana for generating illustrations from up-to-date literature.

FUNDING

Work is part-supported by the Medical Research Council UK (MR/P011292/1) (A.R), and the National Institutes of Health, National Institute of Allergy and Infectious Diseases through Interagency Agreement No. AAI15006 with the Health Resources and Services Administration, Healthcare Systems Bureau, National Hansen's Disease Program (RT, LA). TJK was part-funded by a Wellcome Trust Intermediate Clinical Fellowship (095898/Z/11/Z).

DECLARATION OF INTEREST

TJK undertakes consultancy work for Resolution Therapeutics. All other authors have nothing to declare.

AUTHOR CONTRIBUTIONS:

A.R. conceived the concept and designed the experimental strategy with SH, TJK, DS and MP. SH, TJK, MP, DS, KY, AR analyzed the data. MP selected and organized nine-banded armadillos for the study and collected and analyzed animal data under the supervision of RT, LA and AR. TJK designed and performed the histopathological evaluation and quantification. DS performed machine learning analysis and quantification of the data. SH and KY performed the immunolabeling, imaging and Western blotting. AR, SH and TJK wrote the paper with contributions from MP and DS. All authors read and approved the manuscript.

FIGURE LEGENDS

Figure 1 | *Mycobacterium leprae* promote *in vivo* organ growth of normal liver in adult nine-banded armadillos without hepatic damage.

A, Nine-banded armadillos produce litters of four genetically identical offspring.
B, The parenchyma of all animals has identical echotexture but livers of infected animals are enlarged (right) compared to uninfected animals (left).
C, Confocal images show ML-laden hepatocytes (H) in infected liver detected by ML-specific PGL-1 antibody (red, arrowheads, blue, DAPI) . Inset: Control liver (scale bars 40μm; also see Suppl Fig 1).
D, Eviscerated livers of (a) control, (b) resistant, and (c) infected (19-month example) animals show identical lobation with smooth, uniform outer capsules, organ weight indicated. Scale in field.
E, Scatterplot of bacterial counts vs. liver:body weight for armadillos presented in (a) and (b), with co-efficient of correlation (r), best-fit linear line (red) with confidence interval (grey) ($rs = 0.5775764$, $p = 0.00007687$).
F, Liver:body weight of uninfected (blue), resistant (yellow) and infected animals (red).
G, Bacterial counts (per gram of tissue) in livers from the same control, resistant and infected animals presented in (F).
H, The parenchyma of infected livers (c) is identical to that of uninfected (a) and resistant (b) animals without damage (H&E-stained sections, scale bars 200μm).
I, There is no scarring in infected, (right), uninfected (left), or resistant animals (PSR-stained sections, scale bars 200μm, also see Suppl Fig. 2).
J, Serum levels of liver functional enzymes AST, ALT and LDH, and serum ML-PGL-1 antibody levels, from infected armadillos during the establishment phase of infection compared to controls; anti-PGL level, $p < 0.0001$ (n = number of animals in each group with available test result).

Figure 2 | Bacterial-induced *in vivo* liver organ growth maintains normal hepatic lobular and vascular microarchitecture.

A, Portal tracts and central veins were annotated on digital images of H&E-stained sections (upper) and spatial point patterns (lower) created (representative images, scale shown in lower panels, also see suppl Fig 2).
B, Vascular structures in all groups (n = 13 control, 16 resistant, 15 disseminated) were similarly dispersed without loss of regular arrangement in infected animals (plots of the empirical corrected Ripley's L-function for each group fall below the yellow line representing complete spatial randomness, indicating consistent regularity of vascular structures in all groups).

C, Portal tract density in two-dimensional images was significantly reduced in infected animals compared with control animals, suggesting branch elongation of the biliary fractal geometry (group sizes as in B).
D, The largest 'step' in mean distance in the 6 nearest portal neighbors for every central vein in 13 control animals was between the 3rd and 4th nearest neighbor.
E, Mean modelled lobule size applying the lobule-as-hexagon paradigm, radius derived from the mean of the nearest three portal tracts for each central vein, showed individual lobular size was not increased in the larger livers of infected animals (group sizes as in B).
F, Machine-learning workflow for cell classification.
G, Representative examples of whole sections visible using autofluorescence used for cell-type classification (scale bars, 1 mm). Nuclear signature of hepatocytes (DAPI) and histology of liver sections for cell classification are shown extreme right (arrowheads).
H, DAPI-stained nuclei (top) with matched class (bottom) showing classification accuracy of hepatocytes and non-parenchymal cells (scale bars, 50μm).
I, Representative field from an infected animal showing intact hepatic plates and sinusoidal architecture using autofluorescence (left panel) overlaid with cell-type classification (right panel). Spatial distribution of classified classical hepatocytes (yellow), binucleated hepatocytes (orange), and other (non-parenchymal) cells (purple). Scale bars, 50μm.
J, Superimposed Fite-bacterial stained image of infected liver (left) with classified classical hepatocytes (right) in hepatocyte plates (dotted lines) harboring ML (arrows).
K, Infected liver labelled with HNF4α antibody showing classified classical hepatocytes (a) and binucleate hepatocytes (b; circled) correspond to HNF4α+ hepatocytes (scale bars, 50μm).
L, Density of classical hepatocytes in enlarged livers of infected animals was the same as in uninfected and resistant livers (n = 10 control, 10 resistant, 9 disseminated).
M, Schematic showing significantly enlarged livers have lobules of normal size and normal classical hepatocyte densities, reflecting 'normal' organ growth maintaining normal liver microarchitectural and lobule organization by including matched generative activity from all native cell types and structures.
N, Liver lobules are increased in number but not in size in infected armadillo livers contributing to organ growth, in contrast to pathologically inflated livers with increased liver lobule size.

Figure 3 | The transcriptome of infected nine-banded armadillo livers reflects organ regeneration, reactivation of liver developmental progenitors, growth, and differentiation.

A, Shared, unique annotations for nine-banded armadillo and human protein coding genes with designated gene symbols, showing significant overlap between nine-banded armadillo and human.
B, Waffle diagram of RNAseq detected annotated (purple), detected unannotated (green), and undetected (red) genes out of the total known armadillo protein coding genes.
C, GO terms of functional categories of significantly upregulated genes in infected armadillo liver identified by GSEA analysis in 2-D semantic space, with related terms positioned closer together.
D, Selected upregulated common genes in infected livers are grouped into indicated functional categories related to liver growth and regeneration.
E, Representative H&E staining showing similarities of armadillo (left) and human (right) liver (scale bars, 200um).

F, Schematic of liver lobular structure and major cell types in adult human liver, resembling armadillo liver cell types indicated in (E).

G, Cross-referencing of differentially expressed genes from infected armadillo livers with annotated liver cell types from published scRNAseq from normal adult human liver (Aizarani et al) showing total gene number for each cell type.
H-L, Selection of differentially expressed genes ($p < 0.05$, fold change > 1.5) in heatmaps for indicated individual liver cell types in infected armadillo livers based on human gene homologues in corresponding human liver cell types identified by scRNAseq; highly upregulated and functionally relevant selected genes in each cell type are shown in boxed areas. Expression shown as log FPKM, genes hierarchically clustered according to expression values.

Figure 4 | ML-infected adult armadillo livers are non-fibrotic but pro-regenerative: comparison with human fibrotic liver diseases, human fetal livers and rodent fibrotic and hepatectomy-induced regeneration models.

A, Upregulation of collagens and smooth muscle actin is restricted in non-fibrotic livers of infected armadillo liver compared with the common suite of collagens produced in pro-fibrotic activation of scar-orchestrating cells in mouse fibrotic model.
B, GO terms of common genes upregulated in both the unscarred infected livers and a discrete lineage of scar-orchestrating hepatic stellate cells in a murine model of fibrogenesis induced by chronic injury with carbon tetrachloride includes regenerative, homeostatic and metabolic processes in addition to wounding responses and extracellular matrix production.

C, D, Uninfected armadillo liver (C) has the same sinusoidal organization as the liver of animals infected with ML (D), and increasing duration of infection (up to 795 days) does not induce fibrosis (D-a, -b, -c, picrosirius red (PSR) (scale bars 200 μm).

E, F, Organization of normal adult human liver (E) shows no difference from normal adult nine-banded armadillo liver (C) (H&E and PSR). However, normal architecture is lost in human chronic liver diseases (F); (a) chronic infection with hepatitis C virus (HCV); (b) granulomatous injury (primary biliary cholangitis; PBC), and (c) metabolic injury with lipid accumulation, non-alcoholic fatty liver disease (NAFLD), all leading to extensive scarring and loss of normal vascular relationships representing cirrhosis (scale bars 200 μm).

G, Infected armadillos show upregulation of genes included in sets of hepatic and biliary genes that define populations of fetal and adult hepatocytes (fHep and aHep), fetal and adult hepatobiliary hybrid progenitors (fHHyP and aHHyP), and adult biliary epithelial cells (aBEC) in human liver (Segal et al). Heatmap shows log2FC upregulation in infected livers for genes appear in one or more gene sets used to define epithelial or progenitor cell types. Some genes appear on more than one cell type-defining list; black entries for a stated cell type indicate where the gene does not appear on that cell type-specific list. Selected genes from clusters specifically shared with human fetal liver (indicated by asterisk) are shown inset (see Supl file 2).

H, GO terms of common genes upregulated in both ML-infected livers and defining the EPCAM1+ progenitor cluster in adult human liver (Aizarani et al).

I, GO terms of common genes upregulated in both ML-infected livers and in the livers of rats 24-hours after partial hepatectomy (Colak et al) include those relating to DNA synthesis, subcellular organization, and other proliferation-related terms.

Figure 5 I Reactivation of liver progenitor/development marker proteins with sustained liver functions in infected livers.

A, FOXA1 and FOXA2 genes are significantly upregulated in infected livers. Mean+/- SD from triplicates from two infected and two control armadillos.

B-D, FOXA1 and FOXA2 proteins are reactivated specifically in selected pericentral/midzonal hepatocytes in infected livers in situ (B), but are absent in uninfected adult armadillo (C) and normal human liver (D) (human liver images from Human Protein Atlas).

E, Reactivity of cross-species (mouse/human) antibodies to liver progenitor and other functional markers with total armadillo liver extracts by Western blotting shows upregulation in infected liver. Mouse adult liver (right panel) as positive control.

F, Quantification of protein expression (normalized with beta-actin and alpha-tubulin) for proteins (E). Mean+/- SD from triplicates from three infected and two control armadillos.

G, Confocal immunofluorescent imaging of selected upregulated proteins indicative of functional liver (albumin) and developmental or homeostatic mature hepatocyte activity (E-cadherin, ß-catenin, HNF4α) or proliferation (PCNA). No significant difference in macrophage marker CD68 (scale bars, 50μm).

H, Infected armadillo liver (B, G) is phenotypically similar to normal human adult liver. *In situ* expression of the homologous proteins in human livers adapted from Human Protein Atlas (scale shown).

Figure 6 | Infected livers undergo dynamic in vivo reprogramming, growth and proliferative responses, and activation of regeneration programs while maintaining liver fitness with normal liver zonation and metabolic phenotype

A, B, Genes upregulated in ML infection with shared mapping to GO terms pertinent to aging, regeneration, developmental maturation, liver development and homeostasis, wound healing, cell proliferation and response to growth factors, broadly reflecting tissue growth rejuvenation and regeneration. GO terms also include ERK1/2 cascade, a known ML-induced signaling pathway mediating rodent and human Schwann cell proliferation.

C, The majority of senescence inducing and inhibiting genes identified in the CellAge database of cell senescence genes are not differentially expressed in ML-infected liver.

D, Proliferating cell nuclear antigen (PCNA) positive hepatocytes are increased in infected armadillo livers (left panel and inset; arrows). PCNA+ classical hepatocyte nuclei (arrows) with a corresponding schematic demarcating PCNA+ cell-containing hepatocyte plates (right images).

E, PCNA is significantly transcriptionally upregulated in infected livers. Data from three infected and two control armadillos. Scale bars, 50um

F, Quantitative analysis showing increased numbers of PCNA+ classical hepatocyte nuclei in infected livers. Presented as mean +/- SD from triplicates from three infected and two control armadillos.

H, Expression of functional proteins in mature hepatocytes (Cyp3A4, CPS1, glutamine synthetase (GS) and Cyp2D6) shows the same zonal or panlobular expression in infected and control armadillo liver (scale bars 200μm).

I, A similar zonal pattern of expression is seen in normal human livers (images from the Human Protein Atlas, scale shown).

Figure 7 | A model for bacterial-induced liver organ growth in living animals.

A proposed mechanism of cyclical progenitor and mature/differentiated hepatocyte population generation producing liver growth and allowing intracellular bacterial propagation in the adult liver.

STAR METHODS

RESOURCE AVAILABILITY

Lead contact

Further information and requests for resources and reagents should be directed to and will be fulfilled by the lead contact, Anura Rambukkana (a.rambuka@ed.ac.uk)

Materials Availability

Enquiries regarding this study should be directed to the lead contact. All reagents generated in this study are available from the Lead Contact without restriction.

Data and Code Availability

RNA-sequencing data generated in this study has been deposited to GEO and the accession code included in the Key Resources Table. Whole slide images of H&E stained sections of liver from nine-banded armadillos chronically systemically infected by Mycobacterium leprae, resistant to systemic infection by Mycobacterium leprae, or uninfected and used in this paper (acquired on a Hamamatsu NanoZoomer in. ndpi format) are available at https://doi.org/10.7488/ds/3147. Detailed description of bespoke data analysis methods and pipelines using code are provided within the published article. All other data reported in this paper will be shared by the lead contact upon request without restriction. Any additional information required to reanalyze the data reported in this paper is available from the lead contact upon request.

EXPERIMENTAL MODEL AND SUBJECT DETAILS

Nine-banded armadillo acquisition and preparation

In vivo armadillo studies were undertaken at the United States Department of Health and Human Services, Health Resources and Services Administration, Healthcare Systems Bureau, National Hansen's Disease Program (NHDP), Baton Rouge, Louisiana, USA. Both captive-born (provided by Frank Knight, University of Ozarks, Clarksville, Arkansas) and locally wild caught armadillos were used. In total, 57 armadillos were used in this study, comprising 12 uninfected controls, 13 infected resistant and 32 disseminated animals (Suppl data Table 1). Of these all disseminated, 8 uninfected controls and 9 resistant armadillos were used for liver: body weight analysis presented in Figs. 1a-c and Suppl Fig. 1. In addition, 4 uninfected/controls and 4 resistant animals were used in histological and DAPI screening for machine-learning/computational analyses.

Wild armadillo husbandry

Free ranging armadillos were taken by local trappers and transported to the National Hansens's Disease Program (NHDP) vivarium where they were housed in modified rabbit cages and conditioned for experimental inoculation with viable *M. leprae*. During conditioning the animals were treated for intercurrent bacterial and parasitic infections and adapted to the laboratory environment as follows: 1) the formulary used in armadillo maintenance is highly restricted to 1 antibiotics (ampicillin), 1 antihelminth (ivermectin), and 1 injectable (Detomidine with Xylazine) and 1 gas anaesthesia (isolflourane). None have consequential liver effects. Animals were maintained in captivity for more than 1 year before being infected and all of the non-infected animals were exposed to these same agents as the infected. Thus, the non-infected tissues are appropriate controls for these and other unknown environmental variables

To test if armadillos harboured a pre-existing infection with *M. leprae*, animals were held for 3-6 months and tested twice for serum antibodies to *M. leprae*-specific phenolic glycolipid-1 (PGL-1). After conditioning, the animals were skin tested using Lepromin (a suspension containing 10^7 killed bacilli) to determine the type of granuloma they may form in response to *M. leprae*, and lepromatous/multibacillary animals (armadillos that extensively propagate bacilli in tissues) likely to develop disseminated disease were selected.

Captive-born animal husbandry

Gravid females were caught in the wild and kept in captivity where they gave birth to four genetically identical clonal siblings. The young were brought to the NHDP vivarium at approximately 4 months of age and conditioned for a longer period (up to 2 years depending on size and weight gain) than the wild caught armadillos. During conditioning they were routinely dewormed, treated with antibiotics as described above for intercurrent issues, lepromin tested, and screened for anti-PGL1 antibodies for evidence of any prior *M. leprae* infection.

Ethical approval

The study was approved and conducted within the ethical guidelines outlined under the U.S. Department of Agriculture Animal and Plant Health Inspection Service and the U.S. Public Health Service Policy for the Care and Use of Laboratory Animals (NHDP IACUC assurance number A3032-01). This approval is a part of the interagency agreement by the National Institutes of Health, National Institute of Allergy and Infectious Diseases for providing *in vivo* grown leprosy bacilli and other leprosy research reagents to researchers worldwide [69].

Comparative studies on human liver tissue

Human tissue was obtained by application to the Lothian NRS Human Annotated Bioresource under ethical approval number 15/ES/0094 from East of Scotland Research Ethics Service REC 1 that

authorizes anonymized unconsented access to tissue. Formalin-fixed paraffin-embedded sections of liver with the stated chronic liver diseases, or histologically normal liver in resections for metastatic malignancy, were H&E and PSR stained for illustrative purposes. Anonymized tissue sections were provided by the Bioresource with a diagnosis only (indicated in figure legends), and patient age and gender are not known to the authors.

METHOD DETAILS

Selection of armadillos for disseminated infection by Lepromin test

The Lepromin test determines the histopathological response to *M. leprae* using lepromin, which consists of a suspension of whole, autoclaved *M. leprae* derived from athymic nude mice footpads [39,70] containing phenol as preservative. Lepromin was inoculated intradermally in the abdomen and the area was tattooed for later identification. Three weeks after injection a skin sample was collected using a 6 mm biopsy punch, and the biopsy was fixed in neutral buffered formalin for further processing and Wafe-Fite staining to detect acid-fast bacilli. A negative response to the test is associated with the multibacillary form of leprosy and an inability to mount a T-cell-mediated immune (CMI) response to *M. leprae* (similar to human lepromatous/multibacillary leprosy form) whereas a positive response is indicative of a high CMI-associated granulomatous response and successful elimination of the bacilli (resembling human tuberculoid/paucibacillary leprosy). The majority of the Lepromin test negative armadillos progress to a fully disseminated infection while animals that manifest a Lepromin positive response develop only mild disease. Therefore, only armadillos that did not respond to lepromin, likely to propagate *M. leprae* infection, were used for final inoculation with viable *M. leprae*.

Experimental inoculation with viable *M. leprae*

The *M. leprae* preparation was freshly harvested (<48 hours) from athymic nude mouse footpads, and viability and contamination with other bacteria were determined as previously described [39,70]. We used strains of *M. leprae* from 3 different geographical origins: Thai-53 (Japan), NHDP-63 and NHDP-98 (United States), and BR-4923 (Brazil). These strains exhibit minor genotypic variability but have no known pathological variation among humans [71]. There was no difference in bacterial propagation or liver growth (liver weight: body weight ratio) from infected animals with ML strains. The average age at inoculation was 24 months and the average body weight was 8-10 pounds (4-5 kg). Underweight animals or those demonstrating any other abnormality were excluded from study. Armadillos were anesthetized using a combination of Ketamine (0.6 ml) and Dexdomitor (0.4 ml) given intramuscularly after the skin at the injection site was cleaned with alcohol. The inoculum, which consisted of $1x10^9$ viable *M. leprae*, was injected slowly in the saphenous vein in a maximum volume of 0.5 ml.

Monitoring infection progression

After inoculation, animals were screened serologically by ELISA every three months for PGL-1 and LID1 antibodies (Suppl data Fig. 1). When a positive ELISA assay (Optical Density (OD) >0.700 measured at 540 nm) was detected, the animals were followed on a monthly basis for progression of infection, liver functions and dissemination by serology and blood serum levels of liver function enzymes (Fig. 5h). On average, the infected animals show anti-PGL-1 antibodies at 9 months after *M. leprae* inoculation. By 18-24 months post-inoculation, most animals develop a severe infection with up to 10^{12} recoverable bacilli from a single armadillo (Fig. 1 and Suppl data Fig. 1). The armadillos are usually sacrificed when generalized dissemination of bacilli is reached and the animals show highly positive PGL-1 ELISA. At the time of sacrifice, disseminated animals showed no apparent physical abnormalities. The majority of lepromin-negative armadillos are susceptible to infection with viable *M. leprae*. However, 20% of the animals will resist challenge. The animals are considered resistant if they do not show serum anti-PGL1 antibodies above the cut-off value of 0.700 OD or signs of dissemination after 40 months post-inoculation (Suppl data Fig. 1c). At sacrifice, these animals will show a considerably lower bacterial count in the liver tissue compared to those that disseminate (Fig. 1b, Suppl data Fig. 1c).

Ultrasound imaging of liver of live armadillos during infection

The liver images of live normal, resistant and disseminated *M. leprae*-infected armadillos were generated using an ultrasound composed by a 15 MHz transducer probe connected to a scanner (MicroUS) which in turn is connected to the summit base unit (Cadwell, USA). The animal was anesthetized, placed in a supine position, and the transducer was positioned on the right side of the abdomen directed cranially towards the thorax. The depth was set to 70 mm to compare the size of the liver to other organs and to 50 mm to measure the area of the liver for comparison among animals (Fig. 1d).

Sacrifice and harvest of tissues

Before sacrifice, animals were given Gentamicin and Penicillin as a precaution against low level secondary bacterial contamination. The animals were anesthetized, shaved, and thoroughly cleaned with iodine, alcohol, and sterile water. After euthanization the liver was removed, placed in a sterile jar and weighed before being placed on ice (Suppl data Fig. 1a). Tissue samples were collected and fixed in neutral buffered formalin and RNAlater for histological examination and molecular analyses. Tissues were transported to the laboratory for sterility testing and AFB enumeration and stored at -80°C until use for molecular analyses.

Tinctorial staining

Formaldehyde-fixed armadillo liver tissue was embedded in paraffin blocks, or frozen in O.C.T. compound following PBS washes and overnight 30% sucrose in PBS solution incubation. Sections were cut onto glass slides, using a microtome or cryostat. For Haematoxylin and Eosin (H&E) staining of

armadillo liver, 10 µm paraffin sections were dewaxed and rehydrated, before incubation in ready-made Harris Haematoxylin. Slides were washed in running water, then differentiated for no more than 5 seconds in 1% acid alcohol, before transferring to Scott's tap water substitute. Some sections from frozen armadillo liver were also used in this study. Slides were then stained in eosin solution, washed in running water, dehydrated, cleared in xylene, and then mounted with Pertex and glass coverslips by hand or with Shandon Thermo Scientific™ ClearVue™ Coverslipper. For Picro Sirius Red (PSR) staining, 10 µm paraffin sections on glass slides were dewaxed and rehydrated before placing into PSR solution for 2-4 hours. Slides were then rinsed in 100% IMS, cleared in xylene, and mounted.

Digital slide acquisition and expert histopathological screening

For illustrative figures, images were captured on Zeiss Observer microscope with 20x objective lens capturing tiles regions with Zen software. Whole-slide images of H&E-stained sections were captured on a Hamamatsu NanoZoomer to x20 depth; all whole-slide images are available from University of Edinburgh DataShare repository - https://doi.org/10.7488/ds/3147. All H&E and PSR histologically stained sections were examined by a Consultant Liver Histopathologist (TJK) working at the national liver transplant center, blinded to infection status, and all photomicrographs reproduced in the manuscript were reviewed and quality-assured by TJK. Gold-standard subjective evaluation/slide reporting as routinely undertaken on standard human clinical specimens was provided.

Antibodies, immunolabeling and confocal microscopy

Most of the immunolabeling labelling procedures were adapted from our previous lab protocols (Masaki et al., 2013; Ng *et al.,* 2000). Frozen 10 µm Armadillo liver sections were methanol fixed at -20°C for 15 minutes, washed with PBS, and then blocked with 10% Goat serum or Horse serum in PBS for 1 hour at room temperature. After blocking, sections were incubated with primary antibodies diluted in blocking solution overnight at 4°C. It should be noted that a large number of commercially available antibodies to mouse and human markers were tested in armadillos but only the small number of antibodies that reacted are documented below; none of the antibodies to immune markers showed any activity.

Primary antibodies for immunofluorescence

We used the following antibodies: Albumin (1:100), HNF4α (1:50-1:100), E-cadherin (1:100), PGL-1 (Ng *et al*., 2000) (1:500). Sections were washed in PBS and incubated with secondary antibodies diluted in blocking solution for 90 minutes at room temperature. Secondary antibodies include: Invitrogen AlexaFlour; anti-rabbit 568, anti-mouse 488, anti-rabbit 647, DyLight; anti-goat 549, Sigma; anti-goat 568. Sections were stained with DAPI dilactate, washed with PBS and dH_2O, and mounted under glass coverslips using Fluorsave mounting media. For the detection of macrophages in the liver we generated armadillo specific CD68 antibodies (see below).

Nine-banded armadillo-specific anti-CD68 antibody generation

None of the commercially available antibodies to mouse and human immune markers were reactive with armadillo immune cells. Since macrophages are resident in the liver and are known to play a role during infection and also liver regeneration, we generated polyclonal antibodies specifically directed to a nine-banded armadillo sequence of macrophage marker CD68 which shared with several macrophage subtypes and Kupffer cells, using the services of ProteoGenix (Suppl data Figure 12). The amino acid sequence of the extracellular domain of the nine-banded armadillo with added His-tag, shown below, was used to generate a recombinant armadillo CD68 protein (rCD68) for immunizing rabbits. Armadillo CD68 amino acid sequence used for generating rCD68 is shown below:

MGKDCPHKKSATLLPSFTVTPTATESTASTATASHRTTKSHKTTSHKTTTHRTTTHQPTTHQSTTSPGPTN
ATHNPATTTSHGNATVHPTSNSTTSQGTTSTSSPHPRPPPPSPSPSPGSKEAEGDYTWLNGSQPCIRLQA
QIQIRVLYPTQDGEEAWGISVLNPNKTKAEGECGGAHAHLLLTFPYGQLSFGFKQEPTQGTVYLNYMAME
YNVSFPRTTQWTFLAENASLGDLQAPLGRSFSCRNASIMLSPALHVDLLSLQVQAAQLPPTGVFGPSFSC
PSDQGSHHHHHH

This rCD68 was expressed in *E. coli*, purified from an affinity column and checked for purity by Coomassie blue staining after protein separation by gel electrophoresis. Purity was confirmed as a single band corresponding approximately to a 35 or 37kDa protein. Using the rCD68 as immunogen polyclonal antibodies were raised in two rabbits, with monitoring of serum antibody reactivity to rCD68 by ELISA with OD450nm. These anti-CD68 antibodies were then affinity purified and tested for specific reactivity against 0.5µg rCD68 protein using two antibody dilutions (1:8,000 and 1:16,000) by western blot validation. Subsequently, anti-CD68 antibodies were determined to react specifically in armadillo liver protein extracts from control, 19-, 24- and 30-month infected animals across a range of loading concentrations (20, 50 and 100µg) in western blots, with clear, single bands observed. Specific detection of macrophages was also observed in immunofluorescence in Armadillo livers, as compared to antibody controls (Suppl data Figure 10; also shown in the main Figs. 5a, c).

Immunofluorescence

For some antibodies, antigen retrieval was performed in citrate buffer pH6. Sections were washed sequentially in PBS, PBS 0.1% Triton X-100, PBS 0.01% Triton X-100, PBS, at 4°C, before blocking in 5% goat serum in PBS for 1 hour at room temperature. Sections were incubated in primary antibodies diluted in PBS 0.01% Triton X-100 1% goat serum at 4C overnight. After PBS washes, sections were incubated in secondary antibodies diluted in PBS 0.01% Triton X-100 1% goat serum for 1 hour at room temperature, before DAPI dilactate staining, washing and mounting. Images were captured on a Nikon Eclipse 2100 epifluorescence microscope with 20x objective, an inverted widefield Zeiss Observer

873 microscope with 20x objective, and a Zeiss LSM710 confocal microscope with 40x or 63x objective
874 running Zen software.

875 **Immunohistochemistry**

876 IHC was carried out by the professional histology services of SuRF (QMRI, Edinburgh) on 10 μm frozen
877 Armadillo liver sections. All samples were peroxide blocked followed by primary antibody incubations
878 for 1 hour at room temperature. Primary antibodies used: FOXA1 (1:100), FOXA2 (1:200), PCNA (1:20),
879 CYP2D6, CYP3A4 (1:400), CPS1 (1:1000), GS (1:5000), E-cadherin (1:100). Irrelevant antibodies or
880 primary antibodies that did not react with armadillo tissues were used as negative controls. Primary
881 antibodies were followed by polymer and DAB incubations, hematoxylin counterstain, and mounting
882 with cover glass. All steps included TBST washes in between, and the procedure utilized Bond polymer
883 refine detection. Images were captured on an inverted widefield Zeiss Observer microscope with 20x
884 objective lens and tile scanning, running Zen software, or a Zeiss Axioscan slide scanner microscope.

885 **Oil Red O staining**

886 Oil red O (ORO) staining was performed on frozen 10 μm Armadillo liver sections, according to published
887 methods [72]. As a positive control, sections of steatotic human liver were used. Slides were left to
888 equilibrate for 10 minutes at room temperature, covered with filtered ORO working solution for 5
889 minutes, before washing for 30 minutes with running water. Slides were mounted with Fluorsave and
890 glass coverslips and sealed with nail polish prior to imaging on an Olympus BX61 upright widefield
891 microscope with a 10x objective lens.

892 **Protein extraction and Western blots**

893 Protein lysates were collected from freshly frozen armadillo liver tissue by homogenizing 1 g tissue per
894 20 ml T-PER reagent containing Halt protease inhibitor cocktail. Samples were clarified at 10,000g for
895 5 minutes to the remove tissue debris, and supernatant stored at -80°C until used. Total protein was
896 quantified using BCA assay. Western blotting was performed using our previous described protocol (22,
897 38, 52, 53). Protein lysates and standards were run at appropriate concentration (100μg/lane) with
898 NuPAGE sample buffer, after heat treatment at 95°C for 5 minutes to denature. Proteins were run on
899 pre-cast NuPAGE 4-12% Bis/Tris Gels at 200V in 1x NuPAGE MOPS SDS running buffer containing 0.5
900 ml NuPAGE antioxidant. Proteins were transferred to a membrane in a NuPAGE blotting system and 1x
901 Transfer buffer containing 10-20% methanol, for two hours at 20V. The membrane was then blocked in
902 5% non-fat milk powder in PBS-T (PBS containing 0.5% Tween-20), or in BSA in PBS for 1 hour at room
903 temperature on a rocking platform. Blocking solution was removed, and primary antibodies added
904 diluted in blocking solution or Western blocking reagent.

905 Primary antibodies used in Western blotting include the following: Albumin (1:250), HNF4α
906 (1:100), FOXA2 (1:200), SOX9 (1:100), SOX17 (1:500), GATA6 (1:25), E-cadherin (1:500), β-catenin

(1:2000), CEBP/α (1:100), CD68 (see previous section, 1:100), β-actin (1:3000), α-tubulin (1:3000), MST1 (1:300), MST2 (1:300), SAV1 (1:300), LATS1 (1:300), YAP/TAZ (1:300), IGF1 (1:500). Primary antibody incubation was overnight at 4°C on a benchtop rotator. Following this, the membranes were washed three times for at least 10 minutes each in PBS-T, on a rocking platform. Secondary antibodies, diluted in blocking solution, were added and incubated for 1 hour at room temperature with rocking. Secondary antibodies include: Cell Signaling Technology; anti-mouse HRP (1:3000), anti-rabbit HRP (1:3000), ThermoFisher; anti-goat HRP (1:3000). Membranes were washed three times, 10 minutes each, in PBS-T and then exposed to ECL Prime detection reagents as per manufacturer's instructions. Protein bands were detected using a LI-COR Odyssey Imager using Image Studio software, and bands quantified using Image Studio Lite and Image J.

Analysis of liver functional enzymes in blood samples

Blood serum levels of AST, ALT and LDH were measured using Element DC Veterinary Chemistry. Analyzer, which is a diagnostic medical device that analyses blood by calorimetric assay using DRI-CHEM slides. Analyses were performed according to the manufactures instructions (HESKA). Graphing and statistical analysis of the data was carried out using GraphPad Prism (v8) software.

Hepatic lobular architectural analysis of adult armadillo livers

Whole-slide images of H&E-stained sections were acquired using a Hamamatsu NanoZoomer to x20 depth and exported as .ndpi files. Tiled-TIFF thumbnails were generated from the .ndpi files using ndpisplit from the NDPITools suite [73], and tiled-TIFF files converted to jpeg by command-line ImageMagick for annotation using the FIJI implementation of ImageJ [74,75]. The centre of each central vein and centre of each hepatic artery (identifying portal tracts when paired with a portal vein branch or bile duct) were separately annotated by the pathologist. Analysis of the relative positions of the vascular structures was undertaken in RStudio (R 3.3.2) [76]. For each image, vascular positions were imported using the RImageJROI package read.ijroi() function [77], and converted into spatstat package format using the ij2spatstat() function [78]. The distances from each central vein to the 6 nearest portal tracts were calculated with the nndist function. To estimate individual liver lobule size, based on the classical lobule depiction as a regular hexagon, the mean of the distances from each central vein to the nearest three portal tracts (r) was used to calculate the area:

$$\left(\frac{3\sqrt{3}}{2}\right).r^2$$

The distribution of the vascular structures was determined using Ripley's L-function, as previously described [79].

Tissue staining and processing for hepatic cellular composition analysis

Cellular composition of the armadillo livers was assessed by taking advantage of characteristic hepatocyte nuclear appearances by DAPI nuclear staining and machine learning identification of hepatocytes and non-hepatocytes or other cells. For this analysis, armadillo liver paraffin sections of equal thickness (4 μm) were de-waxed and rehydrated, then incubated in DAPI dilactate diluted in dH_2O, washed in distilled water, and mounted in prolong diamond antifade mountant. All liver samples were processed together at the same time to minimize variability. DAPI-stained liver tissue sections were imaged on a Zeiss Axioscan.Z1 (Carl Zeiss AG, Oberkochen, Germany) at 20x using fluorescence filters configured for DAPI and FITC (to acquire autofluorescence). Whole slide .czi files were imported into TissueStudio 2.4 (Definiens AG, Munich, Germany) for automated tissue detection and nuclear segmentation using Tissue Studio's built-in nuclear detection function. TissueStudio workspaces were then opened in DeveloperXD 2.7 (Definiens AG, Munich, Germany) where the following processing and analysis was conducted: Six 500 X 500pixel regions (1 ROI taken from each of two tissues selected from each animal group) were manually classified for nuclear type by an expert liver pathologist (TJK).

Machine learning algorithm for cell classification: generation and application of a Decision Tree model for quantitative cellular composition analysis

The six classified ground truth, gold-standard, pathologist-scored ROIs were then used to train a decision tree model (7 depth, 1 sample per leaf, 5-fold cross validation) to distinguish between single hepatocyte nuclei and non-hepatocytes (details of model parameters and feature set can be found in Suppl Table 2A). Seventy percent of the pathologist-classified hepatocytes and 70% of the non-hepatocytes were used to train the models (training population), with the remaining 30% of each population used to test the accuracy of the model (test population). Using the features defined in Suppl Table 2A, we were unable to reliably classify binuclear hepatocytes as part of a decision tree model because of the morphological similarities between dense touching non-hepatocyte nuclei and binuclear hepatocyte nuclei and so a decision was taken to first use machine learning to classify hepatocytes vs non-hepatocytes and then to reclassify binuclear cells in a stepwise fashion. Therefore, following classification of cell objects in the training ROIs into hepatocytes and non-hepatocytes, a series of stepwise automated class reassignments based on morphology and object context were then used to reclassify those nuclei to be considered binuclear (see stepwise binuclear reclassification pipeline Suppl Table 2B). Machine-learning-classified cells and their matching manually classified "ground truth" cells in the test population were then compared to generate an error matrix and calculate statistics for each iteration of the decision tree model. The optimal model parameters were determined by choosing the model that most equally balanced the error matrix statistics between training and test populations. The error matrix for the optimal model can be found in Suppl Table 2C. Compared to the test population,

the optimum decision tree model achieved positive and negative predictive values of 0.92 and 0.88, respectively, with sensitivity, specificity, and accuracy of 0.93, 0.88, and 0.91 and we considered these values to be acceptable for whole-tissue quantification. Rule-based stepwise reclassification of hepatocyte nuclei to binuclear, by definition, required no model to be trained and thus there was no set training population. For this reason, accuracy of the reclassification was tested on the entire manually classified ground truth binuclear and non-binuclear populations giving PPV 0.84 and NPV of 0.99 (Suppl Table 2c). After manually removing artefactual ROIs from each sample's whole-slide image, the optimal decision tree model and subsequent binuclear-classification pipeline was applied to all full-size, whole-slide images of liver sections by first detecting the nuclei in Tissue Studio and then applying the processing and machine learning pipeline in Developer XD.

Detailed Machine-Learning Stepwise Workflow for armadillo liver cell classification

Armadillo tissue sections were stained with DAPI and imaged on AxioScan.Z1 whole slide scanner. CZI image files imported into Definiens TissueStudio 2.4 Immunofluorescence Portal. Whole tissue detection (auto-threshold, single tissue options applied) and nuclear detection using TissueStudio's built-in nuclear segmentation tools operating on the DAPI channel (nucleus region = 1, Typical Nucleus Size = 70um^2). The whole batch was then processed together with the same tissue and nuclear detection settings (Sol_DetectNuclei_TS.dax). The resulting TissueStudio Workspace was saved and opened in Definiens DeveloperXD 2.4. One candidate region was selected from each of six images covering the range of tissue and nuclear morphology. Training regions were cropped along with nuclear objects then exported and sent to pathologist. Pathologist manually classified all cells in every region and created coloured masks of nuclear classes using Tissue-Studio-segmented nuclear objects as a mask (ImageJ) (Fig 3A). Coloured class masks were imported into Definiens DeveloperXD workspace. (Sol_createTraining DataAndTrainModels.dcp). Training regions were arranged and fused into a single montage with unclassified nuclear objects intact. (Sol_createTrainingDataAndTrainModels.dcp – execute first do loop sections 1-8). Nuclei in training montage were then classified in DeveloperXD by linking mask colour from pathologist classifications to nuclear classes (Hepatocyte, Binuclear, non-Hepatocyte) to create a Definiens-compatible pathologist-trained set of nuclear objects. (Sol_createTrainingDataAndTrainModels.dcp – execute first do loop sections 9&10) 30% of all pathologist-classed nuclei (537 hepatocyte nuclei, 340 non-hepatocyte nuclei) were classified as a test/validation object and not used in training the model. All training and test objects were copied to a new map onto which the model would be applied ("Test Map"). The following section was repeatedly cycled for iterative training using the Definiens Customer Process "Sol_createTrainingDataAndTrainModels.dcp" (section "train and apply decision tree for morphological and intensity classification max/min").

1 - A decision tree model using the features and metrics described in the Materials and Methods was

trained using the training set of nuclear objects. (Open the configuration window for command "[on elongated, hepatocyteNuc: Classifier: Train…]" in the "train and apply decision tree for morphological and intensity classification max/min" section then set modifiable parameters: Tree Depth, Samples Per Leaf, Cross-fold validation before executing the command)

2 – Nuclear objects on Test Map were converted to a temporary class in preparation for model application (execute command "binuclear, elongated… on NuclearLevel: tempNuc" – resets all nuclear classes to temporary class).

3- The trained model was applied to nuclear objects in Test Map of the nuclear training montage (tempNuc objects) (execute command "tempNuc at NucleusLevel: Classifier: Apply").

4 - error matrix was calculated by comparing each pathologist-classed nucleus object to its matching computer-classed objects in "Test Map" and calculating relevant statistics (execute command: "Compute Stats for Hepatocyte Vs Elongated only").

5 – one modifiable parameter (either depth, or samples per leaf, or cross fold validation) in the decision tree model configuration window was then adjusted incrementally.

6 - model was retrained by going back to step 1

Training was iterated and repeated until the error matrix from the internally cross-validated training set model resulted in values that were balanced when the model was applied to the test data set. That is, the error matrices in both training data set and test data set are as comparable as possible given the possible iterations of configuration parameters. Visual confirmation of results is also agreed by pathologist.

Optimum model error matrix of model applied to training data set and to test/validation data set

	PPV	NPV	Sensitivity	Specificity	Accuracy	falsePos/RealPos	FDR	FNR	FOR
trained cells	0.9668	0.9165	0.9404	0.953	0.9455	0.0323	0.0332	0.0596	0.0835
test cells	0.9239	0.8846	0.9274	0.8794	0.9088	0.0763	0.0761	0.0726	0.1154

Training sample set: 1209 hepatocytes, 829 non-hepatocytes. Validation Set: 537 hepatocytes, 340 non-hepatocytes. Decision tree model was then applied across all tissues onto the nuclei segmented using TissueStudio. (execute Sol_ApplyModelsAndExport.dcp as a batch process)

RNA extraction from armadillo livers

Liver samples previously freshly isolated and stored frozen in RNAlater were thawed prior to use and then homogenized in TRIzol at room temperature. The RNA fraction was collected using chloroform and isopropanol-based extraction. Total RNA was resuspended in distilled, RNase-free water and quantified using a Nanodrop ND-1000 Spectrophotometer.

RNA-sequencing of livers from control and infected armadillos

Triplicate RNA samples isolated from 24-month ML-infected, 30-month ML-infected and two control livers were submitted to Arraystar Inc. (Rockville, USA) services for paired-end RNA-sequencing. 1-2 µg total RNA was used to prepare the sequencing libraries. Library preparation involved oligo (dT) magnetic bead mRNA enrichment, highly strand-specific dUTP method using KAPA Stranded RNA-Seq Library Prep Kit, library size distribution and yield QC with Agilent 2100 Bioanalyzer and by absolute quantification qPCR. To sequence the libraries on the IlluminaNovaSeq 6000 instrument, the barcoded libraries were mixed, denatured to single stranded DNA in NaOH, captured on Illumina flow cell, amplified in situ, and subsequently sequenced for 150 cycles for both ends. Image analysis and base calling were performed using Solexa pipeline v1.8 (Off-Line Base Caller software, v1.8). Sequence quality was examined using the FastQC[80] software (v0.11.7).

For sequencing quality control, raw data files in FASTQ format were generated from the Illumina sequencer and the sequencing quality examined by plotting the quality score for each sample. Quality score Q is logarithmically related to the base-calling error probability (P): Q = -10log10(P). Q30 means the incorrect base calling probability to be 0.001 or 99.9% base calling accuracy, and high-quality data was indicated by the percentage of the number of bases with Q ≥ 30 being greater than 80%. The trimmed reads (trimmed 5', 3'-adaptor bases using cutadapt[81] (v1.17)) were aligned to the reference genome (*Dasypus novemcinctus*, Dasnov3.0, GCA_000208655.2 Ensembl) using Hisat2 software (v2.1.0)[82]. The Ensembl Dasnov3.0, INSDC Assembly GCA_000208655.2 was last updated/patched in May 2016, which is well annotated with 22,711 coding genes. The transcript abundances in FPKM at gene and transcript levels were assembled and computed with StringTie (v1.3.3)[83,84]. The differential gene expression was analysed using R package Ballgown (v2.10.0)[85–87]. The novel genes and transcripts not present in the reference genome/transcriptome were predicted by StringTie and their protein coding potentials were scored by CPAT (v1.2.4)[88].

Bioinformatics and differential expression visualization

Sets of total protein coding genes from human (GRCh38.p13) and armadillo (Dasnov3.0) reference genomes were acquired from Ensembl Biomart, and subsequently filtered for genes annotated with gene symbols for cross-comparison. Total armadillo protein coding genes with and without gene symbol

annotations were queried against all detected genes from RNAseq from any sample and presented as a waffle diagram. Heatmaps of data were produced from sets of differentially expressed genes using pheatmap in R, Python or shell environment (Python and Shell: in-house scripts, Arraystar). For heatmap generation, the log2 transformed FPKM values of the expressed genes were tested by ANOVA across the samples for significant difference in expression ($p <= 0.05$) and selected for unsupervised hierarchical clustering using Euclidean distance measure and the 'average' agglomeration method. The heatmap was scaled row-wise, with the colour scale representing the Z-scores.

Gene ontology analysis was performed using GSEA (Broad Institute, MA) software with differentially expressed genes sets pre-ranked in order of fold change, with minimum gene set sizes set to 10. REVIGO[89] was used to visualize GO terms in bubble diagrams, and chord diagrams of differentially expressed genes related to specific GO annotations were created using GOplot[90]. Selection of functional genes of interest used manual literature searches (PubMed) and gene annotations (GeneCards, NCBI). For the liver cell type gene expression pattern analysis, data sets from[42] were used, specifically the gene expression signatures associated with the distinct clusters identified in that study. Clusters and their gene lists were pooled together into the groups; "hepatocytes", "cholangiocytes/biliary/EPCAM+", "Endothelial/Stellate/MyoFB", "Kupffer" and "NK, NKT and T cell" where possible. These lists were then cross-referenced with the Armadillo liver differentially expressed genes of 30-month infected liver vs. control livers to provide the differentially expressed infected armadillo liver genes potentially associating with particular liver cell types. The top differentially expressed genes in each of these groups, and selected other functional genes of interest, were used to produce heatmaps (software as described above). Common oncogenes and tumour-suppressors were compiled from an independently determined reference list of genes (https://www.arraystar.com/lncpath-cancer-microarrays/) and compared with detected genes in Armadillo liver RNAseq to determine whether those detected were significantly differentially expressed in 24- and 30-month infected Armadillo livers, presented as heatmaps after hierarchical clustering. Differential expression of genes in chronically infected armadillos was compared with the differential expression of genes from a discrete lineage of scar-orchestrating cells in a murine model of fibrogenesis[43]. The common set of differentially genes overexpressed in infected armadillo liver and in scar-orchestrating cells after profibrotic injury was used for GO term analysis using g:profiler(ref) and visualized using REVIGO and with chord diagrams from GOplot(ref). The specific expression of collagen species was examined. Genes differentially-expressed in 30-month infected liver versus uninfected control liver were compared with published gene expression data from putative adult and fetal hepatic progenitors[42,44,45], or with gene expression data from a rat partial hepatectomy model[46], and the common set up genes used for GO term analysis and visualization, as above.

To identify changes in senescence-associated genes in ML-infected armadillo liver, genes significantly up- or down-regulated in infected armadillo livers (versus control) were compared with the genes identified in the CellAge database of cell senescence genes as senescence-inducing or senescence-inhibiting[58].

Quantification and Statistical analysis

For armadillo liver: body weight comparisons, liver enzyme assays and for western blot quantification, labelled positive cell quantification in situ, statistical significance was calculated using two-tailed *t-tests*, with errors bars denoting mean ± SEM. RNAseq data was processed as described, with significance in log2 transformed FPKM values of the expressed genes tested by ANOVA. Boxplots were generated by geom_boxplot in the ggplot2 package in R environment, displaying the median, first and third quartiles, with whiskers extending to the largest or smallest values no further than 1.5x the interquartile range from the third or first quartile, with outlier points beyond this plotted individually. Boxplot data was checked for assumptions allowing parametric testing, with lobule area analysis applying Kruskal-Wallis one-way ANOVA, nuclear density analysis using ANOVA with post-hoc Tukey's.

KEY RESOURCES TABLE

REAGENT or RESOURCE	SOURCE	IDENTIFIER
Antibodies		
Goat anti-mouse Albumin antibody	Bethyl Laboratories	A90-134A
HNF-4 α Antibody (C-19)	Santa Cruz Biotechnology	sc-6556
HNF-4 α Antibody (H-171)	Santa Cruz Biotechnology	sc-8987
E-Cadherin (24E10) Rabbit mAb	Cell Signaling Technology	3195
PGL-1 antibody	Gift from Dr. A. Kolk	N/A
Anti-nine-banded armadillo specific CD68 polyclonal antibodies	Rambukkana lab. This paper	N/A
Anti-FOXA2 antibody	Abcam	ab23630
Recombinant Anti-FOXA1 antibody [EPR10881]	Abcam	ab170933
Anti-Sox9 Antibody	Merck/Millipore	AB5535
Human SOX17 Antibody	R&D Systems	AF1924

Human GATA-6 Antibody	R&D Systems	AF1700
β-Catenin (D10A8) XP® Rabbit mAb	Cell-Signaling Technology	8480
Anti-CEBP Alpha antibody [5B7]	Abcam	ab128482
Monoclonal Anti-β-Actin antibody produced in mouse	Sigma-Aldrich	A2228
α-Tubulin (11H10) Rabbit mAb	Cell-Signaling Technology	2125
MST1 Antibody	Cell-Signaling Technology	3682
MST2 Antibody	Cell-Signaling Technology	3952
SAV1 (D6M6X) Rabbit mAb	Cell-Signaling Technology	13301
LATS1 (C66B5) Rabbit mAb	Cell-Signaling Technology	3477
YAP/TAZ (D24E4) Rabbit mAb	Cell-Signaling Technology	8418
IGF1 antibody	GeneTex	GTX100521
Anti-PCNA Antibody, clone PC10 Anti-PCNA Antibody	Millipore Sigma-Aldrich	MAB424R
Anti-CPS1 Antibody	Abcam	ab3682
Anti-Glutamine Synthetase (GS) Antibody	Abcam	ab49873
Anti-CYP3A4 and CYP2D6 antibodies	Gift from Dr. D. Hay	N/A
Goat anti-Rabbit IgG (H+L) Highly Cross-Adsorbed Secondary Antibody, Alexa Fluor 568	Invitrogen/ ThermoFisher Scientific	A-11036
Goat anti-Mouse IgG (H+L) Highly Cross-Adsorbed Secondary Antibody, Alexa Fluor 488	Invitrogen/ ThermoFisher Scientific	A-11029
Goat anti-Rabbit IgG (H+L) Cross-Adsorbed Secondary Antibody, Alexa Fluor 647	Invitrogen/ ThermoFisher Scientific	A-21244
Anti-goat 549 secondary antibody	DyLight	705-505-003
Anti-Goat IgG (H+L), highly cross-adsorbed, CF™ 568 antibody produced in donkey	Sigma-Aldrich	SAB4600074
Anti-mouse IgG, HRP-linked Antibody	Cell-Signaling Technology	7076

Anti-rabbit IgG, HRP-linked Antibody	Cell-Signaling Technology	7074
Donkey anti-Goat IgG (H+L) Secondary Antibody, HRP	ThermoFisher Scientific	A15999
Bacterial strains		
M. leprae: Thai-53, NHDP-63 and NHDP-98 (United States), and BR-4923 (Brazil) strains.	National Hansen's Disease Program (NHDP), USA	N/A
Biological samples		
Human liver tissue	Lothian NRS Human Annotated Bioresource	N/A
Chemicals, peptides, and recombinant proteins		
RNAlater	Sigma-Aldrich	R0901
Deposited Data		
RNAseq data	This paper	Accession code
Whole-slide images of H&E-stained sections of infected, resistant, and control armadillo liver	The University of Edinburgh DataShare repository	https://doi.org/10.7488/ds/3147
O.C.T. Compound	CellPath	KMA-0100-00A
PBS	Oxoid	BR0014G
Sucrose	Sigma-Aldrich	S5016
Goat serum	Life Technologies	10000C
BOND Polymer Refine Detection	Leica Biosystems	DS9800
Oil Red O	Sigma-Aldrich	00625
FluorSave Reagent	Merck/Millipore	345789
T-PER™ Tissue Protein Extraction Reagent	ThermoFisher Scientific	78510
Halt™ Protease Inhibitor Cocktail (100X)	ThermoFisher Scientific	87786
BCA Protein Assay Kit	Boster	AR0146
SeeBlue™ Plus2 Pre-stained Protein Standard	ThermoFisher Scientific	LC5925

NuPAGE™ LDS Sample Buffer	Invitrogen/ ThermoFisher Scientific	NP0007
NuPAGE™ 4 to 12%, Bis-Tris, 1.5 mm, Mini Protein Gel, 10-well	Invitrogen/ ThermoFisher Scientific	NP0335BOX
NuPAGE™ MOPS SDS Running Buffer (20X)	Invitrogen/ ThermoFisher Scientific	NP0001
NuPAGE™ Antioxidant	Invitrogen/ ThermoFisher Scientific	NP0005
Immobilon-P PVDF Membrane	Merck/Millipore	IPVH00010
NuPAGE™ Transfer Buffer (20X)	Invitrogen/ ThermoFisher Scientific	NP0006
Methanol	Fisher Scientific	M/3900/17
Nonfat Dry Milk	Cell-Signaling Technology	9999
TWEEN® 20	Sigma-Aldrich	P1379
Western Blocker™ Solution	Sigma-Aldrich	W0138
Recombinant armadillo CD68 protein (rCD68)	This paper	N/A
Triton™ X-100	Sigma-Aldrich	X100
Amersham ECL Prime Western Blotting Detection Reagent	GE Healthcare	RPN2232
DAPI (4',6-Diamidino-2-Phenylindole, Dilactate)	Invitrogen/ ThermoFisher Scientific	D3571
ProLong™ Diamond Antifade Mountant	Invitrogen/ ThermoFisher Scientific	P36965
TRIzol™ Reagent	Invitrogen/ ThermoFisher Scientific	15596026
Chloroform Pure	Scientific Laboratory Supplies	CHE1576
2-Propanol	Sigma-Aldrich	I9516

Experimental models: Organisms/strains		
Nine-banded Armadillo (*Dasypus novemcinctus*)	National Hansen's Disease Program (NHDP), USA	N/A
Mycobacterium leprae strains: THAI53, Brazil, NHDP63 and NHDP98	National Hansen's Disease Program (NHDP), USA	N/A
Software and algorithms		
Zen software	Zeiss	https://www.zeiss.com/microscopy/int/products/microscope-software/zen-lite.html
Image Studio Lite	LI-COR	https://www.licor.com/bio/image-studio-lite/download
Image J/Fiji	[74,75]	https://imagej.net/Fiji
GraphPad Prism (v8)	GraphPad	https://www.graphpad.com/scientific-software/prism/
RStudio (R 3.3.3)	R Core Team, 2016	https://www.rstudio.com/
TissueStudio 2.4 (Definiens AG, Munich, Germany)	Definiens	

DeveloperXD 2.7 (Definiens AG, Munich, Germany	Definiens	
Solexa pipeline v1.8 (Off-Line Base Caller software, v1.8)		
FastQC software (v0.11.7)	[80]	
cutadapt (v1.17)	[81]	
Hisat2 software (v2.1.0)	[82]	
StringTie (v1.3.3)	[83,84]	
Ballgown (v2.10.0)	[85–87]	
CPAT (v1.2.4)	[88]	
GSEA	Broad Institute, MA	https://www.gsea-msigdb.org/gsea/index.jsp
REVIGO	[89]	
GOplot	[90]	
In situ expression of proteins from normal human liver presented in this study is adapted from the Human Protein Atlas	The Human Protein Atlas Project:	https://v15.proteinatlas.org/about/project [91]

SUPPLEMENTAL DATA ITEMS

Supplemental information includes 11 supplemental figures, 5 tables and 2 supplemental files can be found as separate documents

The supplemental files:

1. **Data S1:** Differentially expressed genes in ML-infected versus control armadillo liver based on cell type specific annotation from scRNA-seq data from adult human liver [42]. Related to Fig. 3, 4

2. **Data S2:** GO terms returned by g:GOSt analysis from g:Profiler for shared genes differentially-expressed in ML-infected versus control armadillo liver and also defining EPCAM+ adult

human liver progenitor cluster 4 from Aizarani et al or AFP+ adult human progenitors from MacParland et al. [42, 44] . Related to Fig 3, 4.

REFERENCES

1. Jopling, C., Boue, S., and Belmonte, J.C.I. (2011). Dedifferentiation, transdifferentiation and reprogramming: three routes to regeneration. Nat Rev Mol Cell Biol *12*, 79–89. 10.1038/nrm3043.

2. Rustad, K.C., Sorkin, M., Levi, B., Longaker, M.T., and Gurtner, G.C. (2010). Strategies for organ level tissue engineering. Organogenesis *6*, 151–157. 10.4161/org.6.3.12139.

3. Wells, J.M., and Watt, F.M. (2018). Diverse mechanisms for endogenous regeneration and repair in mammalian organs. Nature *557*, 322–328. 10.1038/s41586-018-0073-7.

4. Clevers, H. (2016). Modeling Development and Disease with Organoids. Cell *165*, 1586–1597. 10.1016/j.cell.2016.05.082.

5. Marsee, A., Roos, F.J.M., Verstegen, M.M.A., Marsee, A., Roos, F., Verstegen, M., Clevers, H., Vallier, L., Takebe, T., Huch, M., et al. (2021). Building consensus on definition and nomenclature of hepatic, pancreatic, and biliary organoids. Cell Stem Cell *28*, 816–832. 10.1016/j.stem.2021.04.005.

6. Cordero-Espinoza, L., and Huch, M. (2018). The balancing act of the liver: tissue regeneration versus fibrosis. J Clin Invest *128*, 85–96. 10.1172/JCI93562.

7. Michalopoulos, G.K., and Bhushan, B. (2021). Liver regeneration: biological and pathological mechanisms and implications. Nat Rev Gastroenterol Hepatol *18*, 40–55. 10.1038/s41575-020-0342-4.

8. Trautwein, C., Friedman, S.L., Schuppan, D., and Pinzani, M. (2015). Hepatic fibrosis: Concept to treatment. Journal of Hepatology *62*, S15–S24. 10.1016/j.jhep.2015.02.039.

9. Llovet, J.M., Zucman-Rossi, J., Pikarsky, E., Sangro, B., Schwartz, M., Sherman, M., and Gores, G. (2016). Hepatocellular carcinoma. Nat Rev Dis Primers *2*, 1–23. 10.1038/nrdp.2016.18.

10. Scheel, T.K.H., and Rice, C.M. (2013). Understanding the hepatitis C virus life cycle paves the way for highly effective therapies. Nat Med *19*, 837–849. 10.1038/nm.3248.

11. Asrani, S.K., Larson, J.J., Yawn, B., Therneau, T.M., and Kim, W.R. (2013). Underestimation of liver-related mortality in the United States. Gastroenterology *145*, 375-382.e2. 10.1053/j.gastro.2013.04.005.

12. Asrani, S.K., Devarbhavi, H., Eaton, J., and Kamath, P.S. (2019). Burden of liver diseases in the world. Journal of Hepatology *70*, 151–171. 10.1016/j.jhep.2018.09.014.

13. Kim, H., Kisseleva, T., and Brenner, D.A. (2015). Aging and liver disease. Curr Opin Gastroenterol *31*, 184–191. 10.1097/MOG.0000000000000176.

14. Allaire, M., and Gilgenkrantz, H. (2020). The aged liver: Beyond cellular senescence. Clinics and Research in Hepatology and Gastroenterology *44*, 6–11. 10.1016/j.clinre.2019.07.011.

15. Morsiani, C., Bacalini, M.G., Santoro, A., Garagnani, P., Collura, S., D'Errico, A., de Eguileor, M., Grazi, G.L., Cescon, M., Franceschi, C., et al. (2019). The peculiar aging of human liver: A geroscience perspective within transplant context. Ageing Research Reviews *51*, 24–34. 10.1016/j.arr.2019.02.002.

16. Forbes, S.J., and Newsome, P.N. (2016). Liver regeneration — mechanisms and models to clinical application. Nat Rev Gastroenterol Hepatol *13*, 473–485. 10.1038/nrgastro.2016.97.

17. Michalopoulos, G.K. (2017). Hepatostat: Liver regeneration and normal liver tissue maintenance. Hepatology *65*, 1384–1392. 10.1002/hep.28988.

18. Takahashi, K., and Yamanaka, S. (2006). Induction of pluripotent stem cells from mouse embryonic and adult fibroblast cultures by defined factors. Cell *126*, 663–676. 10.1016/j.cell.2006.07.024.

19. Hishida, T., Yamamoto, M., Hishida-Nozaki, Y., Shao, C., Huang, L., Wang, C., Shojima, K., Xue, Y., Hang, Y., Shokhirev, M., et al. (2022). In vivo partial cellular reprogramming enhances liver plasticity and regeneration. Cell Reports *39*, 110730. 10.1016/j.celrep.2022.110730.

20. Chen, Y., Lüttmann, F.F., Schoger, E., Schöler, H.R., Zelarayán, L.C., Kim, K.-P., Haigh, J.J., Kim, J., and Braun, T. (2021). Reversible reprogramming of cardiomyocytes to a fetal state drives heart regeneration in mice. Science *373*, 1537–1540. 10.1126/science.abg5159.

21. Lu, Y., Brommer, B., Tian, X., Krishnan, A., Meer, M., Wang, C., Vera, D.L., Zeng, Q., Yu, D., Bonkowski, M.S., et al. (2020). Reprogramming to recover youthful epigenetic information and restore vision. Nature *588*, 124–129. 10.1038/s41586-020-2975-4.

22. Wang, C., Rabadan Ros, R., Martinez-Redondo, P., Ma, Z., Shi, L., Xue, Y., Guillen-Guillen, I., Huang, L., Hishida, T., Liao, H.-K., et al. (2021). In vivo partial reprogramming of myofibers promotes muscle regeneration by remodeling the stem cell niche. Nat Commun *12*, 3094. 10.1038/s41467-021-23353-z.

23. Gill, D., Parry, A., Santos, F., Okkenhaug, H., Todd, C.D., Hernando-Herraez, I., Stubbs, T.M., Milagre, I., and Reik, W. (2022). Multi-omic rejuvenation of human cells by maturation phase transient reprogramming. eLife *11*, e71624. 10.7554/eLife.71624.

24. Abad, M., Mosteiro, L., Pantoja, C., Cañamero, M., Rayon, T., Ors, I., Graña, O., Megías, D., Domínguez, O., Martínez, D., et al. (2013). Reprogramming in vivo produces teratomas and iPS cells with totipotency features. Nature *502*, 340–345. 10.1038/nature12586.

25. Rambukkana, A., Zanazzi, G., Tapinos, N., and Salzer, J.L. (2002). Contact-dependent demyelination by Mycobacterium leprae in the absence of immune cells. Science *296*, 927–931. 10.1126/science.1067631.

26. Tapinos, N., and Rambukkana, A. (2005). Insights into regulation of human Schwann cell proliferation by Erk1/2 via a MEK-independent and p56Lck-dependent pathway from leprosy bacilli. Proceedings of the National Academy of Sciences *102*, 9188–9193. 10.1073/pnas.0501196102.

27. Noon, L.A., and Lloyd, A.C. (2005). Hijacking the ERK signaling pathway: Mycobacterium leprae shuns MEK to drive the proliferation of infected Schwann cells. Sci STKE *2005*, pe52. 10.1126/stke.3092005pe52.

28. Tapinos, N., Ohnishi, M., and Rambukkana, A. (2006). ErbB2 receptor tyrosine kinase signaling mediates early demyelination induced by leprosy bacilli. Nat Med *12*, 961–966. 10.1038/nm1433.

29. Masaki, T., Qu, J., Cholewa-Waclaw, J., Burr, K., Raaum, R., and Rambukkana, A. (2013). Reprogramming Adult Schwann Cells to Stem Cell-like Cells by Leprosy Bacilli Promotes Dissemination of Infection. Cell *152*, 51–67. 10.1016/j.cell.2012.12.014.

30. Hess, S., and Rambukkana, A. (2019). Cell Biology of Intracellular Adaptation of Mycobacterium leprae in the Peripheral Nervous System. Microbiology Spectrum *7*, 7.4.13. 10.1128/microbiolspec.BAI-0020-2019.

31. Cole, S.T., Eiglmeier, K., Parkhill, J., James, K.D., Thomson, N.R., Wheeler, P.R., Honoré, N., Garnier, T., Churcher, C., Harris, D., et al. (2001). Massive gene decay in the leprosy bacillus. Nature *409*, 1007–1011. 10.1038/35059006.

32. Ng, V., Zanazzi, G., Timpl, R., Talts, J.F., Salzer, J.L., Brennan, P.J., and Rambukkana, A. (2000). Role of the Cell Wall Phenolic Glycolipid-1 in the Peripheral Nerve Predilection of Mycobacterium leprae. Cell *103*, 511–524. 10.1016/S0092-8674(00)00142-2.

33. Rambukkana, A. (2010). Usage of signaling in neurodegeneration and regeneration of peripheral nerves by leprosy bacteria. Progress in Neurobiology *91*, 102–107. 10.1016/j.pneurobio.2009.12.002.

34. Rambukkana, A., Salzer, J.L., Yurchenco, P.D., and Tuomanen, E.I. (1997). Neural Targeting of Mycobacterium leprae Mediated by the G Domain of the Laminin-α2 Chain. Cell *88*, 811–821. 10.1016/S0092-8674(00)81927-3.

35. Hess, S., and Rambukkana, A. (2015). Bacterial-induced cell reprogramming to stem cell-like cells: new premise in host–pathogen interactions. Current Opinion in Microbiology *23*, 179–188. 10.1016/j.mib.2014.11.021.

36. Truman, R.W., Ebenezer, G.J., Pena, M.T., Sharma, R., Balamayooran, G., Gillingwater, T.H., Scollard, D.M., McArthur, J.C., and Rambukkana, A. (2014). The Armadillo as a Model for Peripheral Neuropathy in Leprosy. ILAR J *54*, 304–314. 10.1093/ilar/ilt050.

37. Balamayooran, G., Pena, M., Sharma, R., and Truman, R.W. (2015). The armadillo as an animal model and reservoir host for Mycobacterium leprae. Clinics in Dermatology *33*, 108–115. 10.1016/j.clindermatol.2014.07.001.

38. Kirchheimer, W.F., and Storrs, E.E. (1971). Attempts to establish the armadillo (Dasypus novemcinctus Linn.) as a model for the study of leprosy. I. Report of lepromatoid leprosy in an experimentally infected armadillo. Int J Lepr Other Mycobact Dis *39*, 693–702.

39. Truman, R.W., and Krahenbuhl, J.L. (2001). Viable M. leprae as a research reagent. Int. J. Lepr. Other Mycobact. Dis. *69*, 1–12.

40. Truman, R.W., Singh, P., Sharma, R., Busso, P., Rougemont, J., Paniz-Mondolfi, A., Kapopoulou, A., Brisse, S., Scollard, D.M., Gillis, T.P., et al. (2011). Probable Zoonotic Leprosy in the Southern United States. New England Journal of Medicine *364*, 1626–1633. 10.1056/NEJMoa1010536.

41. Teutsch, H.F., Schuerfeld, D., and Groezinger, E. (1999). Three-dimensional reconstruction of parenchymal units in the liver of the rat. Hepatology *29*, 494–505. 10.1002/hep.510290243.

42. Aizarani, N., Saviano, A., Sagar, null, Mailly, L., Durand, S., Herman, J.S., Pessaux, P., Baumert, T.F., and Grün, D. (2019). A human liver cell atlas reveals heterogeneity and epithelial progenitors. Nature *572*, 199–204. 10.1038/s41586-019-1373-2.

43. Kendall, T.J., Duff, C.M., Boulter, L., Wilson, D.H., Freyer, E., Aitken, S., Forbes, S.J., Iredale, J.P., and Hastie, N.D. (2019). Embryonic mesothelial-derived hepatic lineage of quiescent and heterogenous scar-orchestrating cells defined but suppressed by WT1. Nat Commun *10*, 4688. 10.1038/s41467-019-12701-9.

44. MacParland, S.A., Liu, J.C., Ma, X.-Z., Innes, B.T., Bartczak, A.M., Gage, B.K., Manuel, J., Khuu, N., Echeverri, J., Linares, I., et al. (2018). Single cell RNA sequencing of human liver reveals distinct intrahepatic macrophage populations. Nature Communications *9*, 4383. 10.1038/s41467-018-06318-7.

45. Segal, J.M., Kent, D., Wesche, D.J., Ng, S.S., Serra, M., Oulès, B., Kar, G., Emerton, G., Blackford, S.J.I., Darmanis, S., et al. (2019). Single cell analysis of human foetal liver captures the transcriptional profile of hepatobiliary hybrid progenitors. Nat Commun *10*, 3350. 10.1038/s41467-019-11266-x.

46. Colak, D., Al-Harazi, O., and Mustafa, O.M. (2020). RNA-Seq transcriptome profiling in three liver regeneration models in rats: comparative analysis of partial hepatectomy, ALLPS, and PVL. Sci Rep *10*, 5213. 10.1038/s41598-020-61826-1.

47. Le lay, J., and Kaestner, K.H. (2010). The Fox Genes in the Liver: From Organogenesis to Functional Integration. Physiological Reviews *90*, 1–22. 10.1152/physrev.00018.2009.

48. Lee, C.S., Friedman, J.R., Fulmer, J.T., and Kaestner, K.H. (2005). The initiation of liver development is dependent on Foxa transcription factors. Nature *435*, 944–947. 10.1038/nature03649.

49. Reizel, Y., Morgan, A., Gao, L., Lan, Y., Manduchi, E., Waite, E.L., Wang, A.W., Wells, A., and Kaestner, K.H. (2020). Collapse of the hepatic gene regulatory network in the absence of FoxA factors. Genes Dev *34*, 1039–1050. 10.1101/gad.337691.120.

50. Yi, J., Xiong, W., Gong, X., Bellister, S., Ellis, L.M., and Liu, Q. (2013). Analysis of LGR4 Receptor Distribution in Human and Mouse Tissues. PLOS ONE *8*, e78144. 10.1371/journal.pone.0078144.

51. Planas-Paz, L., Orsini, V., Boulter, L., Calabrese, D., Pikiolek, M., Nigsch, F., Xie, Y., Roma, G., Donovan, A., Marti, P., et al. (2016). The RSPO-LGR4/5-ZNRF3/RNF43 module controls liver zonation and size. Nat Cell Biol *18*, 467–479. 10.1038/ncb3337.

52. Michalopoulos, G.K. (2007). Liver regeneration. Journal of Cellular Physiology *213*, 286–300. 10.1002/jcp.21172.

53. Lara-Diaz, V., Castilla-Cortazar, I., Martín-Estal, I., García-Magariño, M., Aguirre, G., Puche, J., de la Garza, R., Morales, L., and Muñoz, U. (2017). IGF-1 modulates gene expression of proteins involved in inflammation, cytoskeleton, and liver architecture. J Physiol Biochem *73*, 245–258. 10.1007/s13105-016-0545-x.

54. Takahashi, Y. (2017). The Role of Growth Hormone and Insulin-Like Growth Factor-I in the Liver. International Journal of Molecular Sciences *18*, 1447. 10.3390/ijms18071447.

55. Patel, S.H., Camargo, F.D., and Yimlamai, D. (2017). Hippo Signaling in the Liver Regulates Organ Size, Cell Fate, and Carcinogenesis. Gastroenterology *152*, 533–545. 10.1053/j.gastro.2016.10.047.

56. Fujita, T., Shirasawa, T., Uchida, K., and Maruyama, N. (1996). Gene regulation of senescence marker protein-30 (SMP30): coordinated up-regulation with tissue maturation and gradual down-regulation with aging. Mech. Ageing Develop *87*, 219–229.

57. Calcinotto, A., Kohli, J., Zagato, E., Pellegrini, L., Demaria, M., and Alimonti, A. (2019). Cellular Senescence: Aging, Cancer, and Injury. Physiol Rev *99*, 1047–1078. 10.1152/physrev.00020.2018.

58. Avelar, R.A., Ortega, J.G., Tacutu, R., Tyler, E.J., Bennett, D., Binetti, P., Budovsky, A., Chatsirisupachai, K., Johnson, E., Murray, A., et al. (2020). A multidimensional systems biology analysis of cellular senescence in aging and disease. Genome Biol *21*, 91. 10.1186/s13059-020-01990-9.

59. Ehrt, S., Schnappinger, D., and Rhee, K.Y. (2018). Metabolic principles of persistence and pathogenicity in Mycobacterium tuberculosis. Nat Rev Microbiol *16*, 496–507. 10.1038/s41579-018-0013-4.

60. Villanueva, A. (2019). Hepatocellular Carcinoma. N Engl J Med *380*, 1450–1462. 10.1056/NEJMra1713263.

61. Donation, G.O. and Transplantation (2016). Organ Donation and Transplantation Activities 2016.

62. Ebenezer, G.J., Pena, M.T., Daniel, A.S., Truman, R.W., Adams, L., Duthie, M.S., Wagner, K., Zampino, S., Tolf, E., Tsottles, D., et al. (2022). Mycobacterium leprae induces Schwann cell proliferation and migration in a denervated milieu following intracutaneous excision axotomy in nine-banded armadillos. Experimental Neurology *352*, 114053. 10.1016/j.expneurol.2022.114053.

63. He, L., Pu, W., Liu, X., Zhang, Z., Han, M., Li, Y., Huang, X., Han, X., Li, Y., Liu, K., et al. (2021). Proliferation tracing reveals regional hepatocyte generation in liver homeostasis and repair. Science *371*. 10.1126/science.abc4346.

64. Wei, Y., Wang, Y.G., Jia, Y., Li, L., Yoon, J., Zhang, S., Wang, Z., Zhang, Y., Zhu, M., Sharma, T., et al. (2021). Liver homeostasis is maintained by midlobular zone 2 hepatocytes. Science *371*. 10.1126/science.abb1625.

65. Dhanasekaran, R., Deutzmann, A., Mahauad-Fernandez, W.D., Hansen, A.S., Gouw, A.M., and Felsher, D.W. (2022). The MYC oncogene - the grand orchestrator of cancer growth and immune evasion. Nat Rev Clin Oncol *19*, 23–36. 10.1038/s41571-021-00549-2.

66. Wuebben, E.L., and Rizzino, A. (2017). The dark side of SOX2: cancer - a comprehensive overview. Oncotarget *8*, 44917–44943. 10.18632/oncotarget.16570.

67. David, R. (2013). Mycobacterium leprae turns back the clock. Nat Rev Mol Cell Biol *14*, 131–131. 10.1038/nrm3526.

68. David, R. (2013). Cellular microbiology: Mycobacterium leprae turns back the clock. Nat Rev Microbiol *11*, 145. 10.1038/nrmicro2975.

69. Hazbón, M.H., Rigouts, L., Schito, M., Ezewudo, M., Kudo, T., Itoh, T., Ohkuma, M., Kiss, K., Wu, L., Ma, J., et al. (2018). Mycobacterial biomaterials and resources for researchers. Pathog Dis *76*. 10.1093/femspd/fty042.

70. Job, C.K., and Truman, R.W. (2000). Comparative study of Mitsuda reaction to nude mouse and armadillo lepromin preparations using nine-banded armadillos. Int. J. Lepr. Other Mycobact. Dis. *68*, 18–22.

71. Sharma, R., Singh, P., Pena, M., Subramanian, R., Chouljenko, V., Kim, J., Kim, N., Caskey, J., Baudena, M.A., Adams, L.B., et al. (2018). Differential growth of Mycobacterium leprae strains (SNP genotypes) in armadillos. Infect. Genet. Evol. *62*, 20–26. 10.1016/j.meegid.2018.04.017.

72. Mehlem, A., Hagberg, C.E., Muhl, L., Eriksson, U., and Falkevall, A. (2013). Imaging of neutral lipids by oil red O for analyzing the metabolic status in health and disease. Nat Protoc *8*, 1149–1154. 10.1038/nprot.2013.055.

73. Deroulers, C., Ameisen, D., Badoual, M., Gerin, C., Granier, A., and Lartaud, M. (2013). Analyzing huge pathology images with open source software. Diagn Pathol *8*, 92. 10.1186/1746-1596-8-92.

74. Rueden, C.T., Schindelin, J., Hiner, M.C., DeZonia, B.E., Walter, A.E., Arena, E.T., and Eliceiri, K.W. (2017). ImageJ2: ImageJ for the next generation of scientific image data. BMC Bioinformatics *18*. 10.1186/s12859-017-1934-z.

75. Schindelin, J., Arganda-Carreras, I., Frise, E., Kaynig, V., Longair, M., Pietzsch, T., Preibisch, S., Rueden, C., Saalfeld, S., Schmid, B., et al. (2012). Fiji: an open-source platform for biological-image analysis. Nat Meth *9*, 676–682. 10.1038/nmeth.2019.

76. R Core Team (2016). R: A language and environment for statistical computing.

77. Sterratt, D.C., and Vihtakari, M. (2015). RImageJROI: Read “ImageJ” Region of Interest (ROI) Files.

78. Baddeley, A., Rubak, E., and Turner, R. (2015). Spatial Point Patterns: Methodology and Applications with R (Chapman and Hall/CRC).

79. Kendall, T.J., Duff, C.M., Thomson, A.M., and Iredale, J.P. (2020). Integration of geoscience frameworks into digital pathology analysis permits quantification of microarchitectural relationships in histological landscapes. Scientific Reports *10*, 17572. 10.1038/s41598-020-74691-9.

80. Andrews, S., Krueger, F., Segonds-Pichon, A., Biggins, L., Krueger, C., and Wingett, S. (2012). FastQC. http://www.bioinformatics.bbsrc.ac.uk/projects/fastqc.

81. Martin, M. (2011). Cutadapt removes adapter sequences from high-throughput sequencing reads. EMBnet.journal *17*, 10–12. 10.14806/ej.17.1.200.

82. Kim, D., Langmead, B., and Salzberg, S.L. (2015). HISAT: a fast spliced aligner with low memory requirements. Nat. Methods *12*, 357–360. 10.1038/nmeth.3317.

83. Mortazavi, A., Williams, B.A., McCue, K., Schaeffer, L., and Wold, B. (2008). Mapping and quantifying mammalian transcriptomes by RNA-Seq. Nat. Methods *5*, 621–628. 10.1038/nmeth.1226.

84. Pertea, M., Pertea, G.M., Antonescu, C.M., Chang, T.-C., Mendell, J.T., and Salzberg, S.L. (2015). StringTie enables improved reconstruction of a transcriptome from RNA-seq reads. Nat. Biotechnol. *33*, 290–295. 10.1038/nbt.3122.

85. Frazee, A.C., Pertea, G., Jaffe, A.E., Langmead, B., Salzberg, S.L., and Leek, J.T. (2014). Flexible analysis of transcriptome assemblies with Ballgown. bioRxiv, 003665. 10.1101/003665.

86. Frazee, A.C., Pertea, G., Jaffe, A.E., Langmead, B., Salzberg, S.L., and Leek, J.T. (2015). Ballgown bridges the gap between transcriptome assembly and expression analysis. Nat. Biotechnol. *33*, 243–246. 10.1038/nbt.3172.

87. Pertea, M., Kim, D., Pertea, G.M., Leek, J.T., and Salzberg, S.L. (2016). Transcript-level expression analysis of RNA-seq experiments with HISAT, StringTie and Ballgown. Nat Protoc *11*, 1650–1667. 10.1038/nprot.2016.095.

88. Wang, L., Park, H.J., Dasari, S., Wang, S., Kocher, J.-P., and Li, W. (2013). CPAT: Coding-Potential Assessment Tool using an alignment-free logistic regression model. Nucleic Acids Res. *41*, e74. 10.1093/nar/gkt006.

89. Supek, F., Bošnjak, M., Škunca, N., and Šmuc, T. (2011). REVIGO Summarizes and Visualizes Long Lists of Gene Ontology Terms. PLOS ONE *6*, e21800. 10.1371/journal.pone.0021800.

90. Walter, W., Sánchez-Cabo, F., and Ricote, M. (2015). GOplot: an R package for visually combining expression data with functional analysis. Bioinformatics *31*, 2912–2914. 10.1093/bioinformatics/btv300.

91. Uhlén, M., Fagerberg, L., Hallström, B.M., Lindskog, C., Oksvold, P., Mardinoglu, A., Sivertsson, Å., Kampf, C., Sjöstedt, E., Asplund, A., et al. (2015). Proteomics. Tissue-based map of the human proteome. Science *347*, 1260419. 10.1126/science.1260419.

92. Learning from exotic species. (2013) Cell *154*, 257-258.

MAIN FIGURES & FIGURE LEGENDS

Figure 1

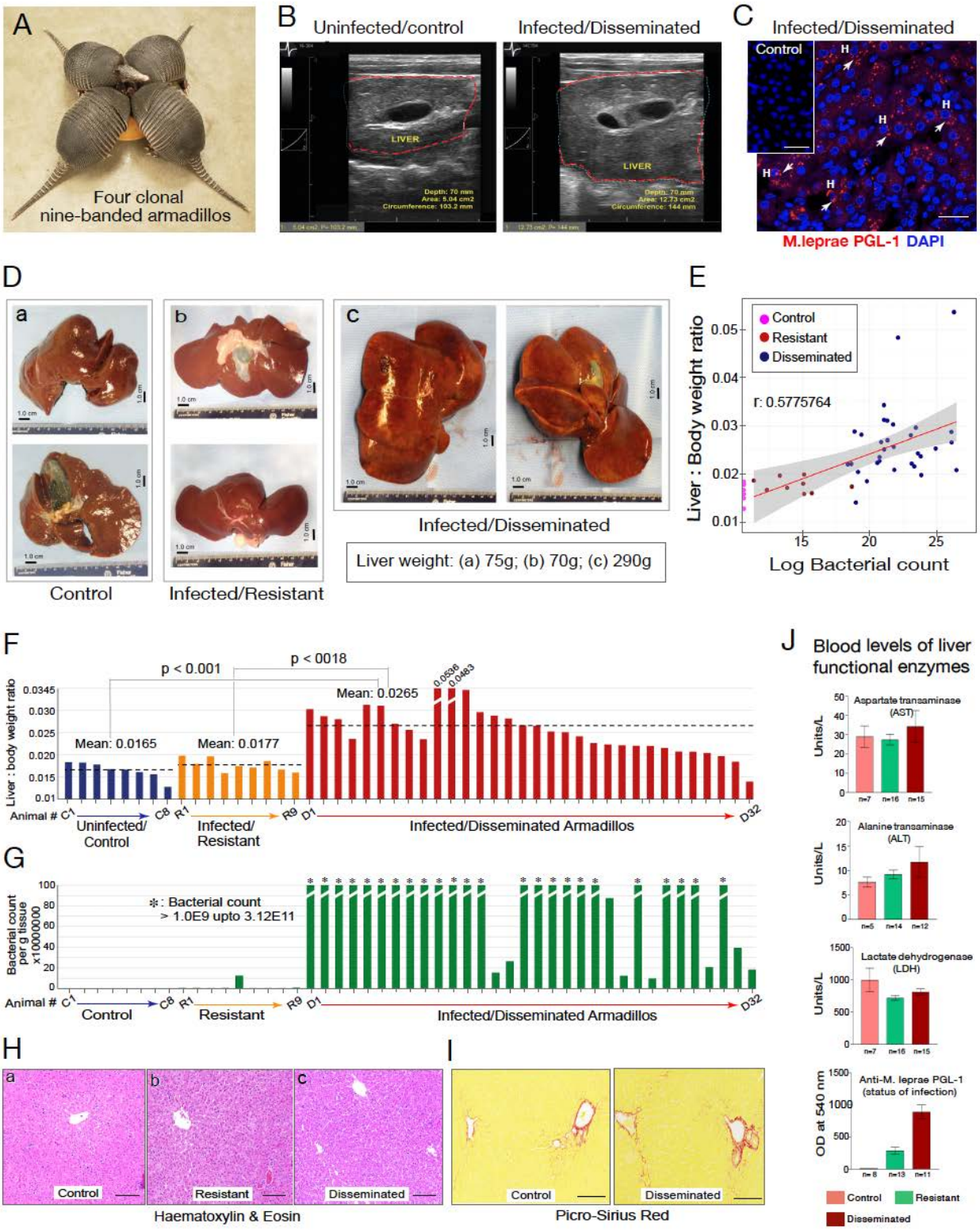

Figure 2

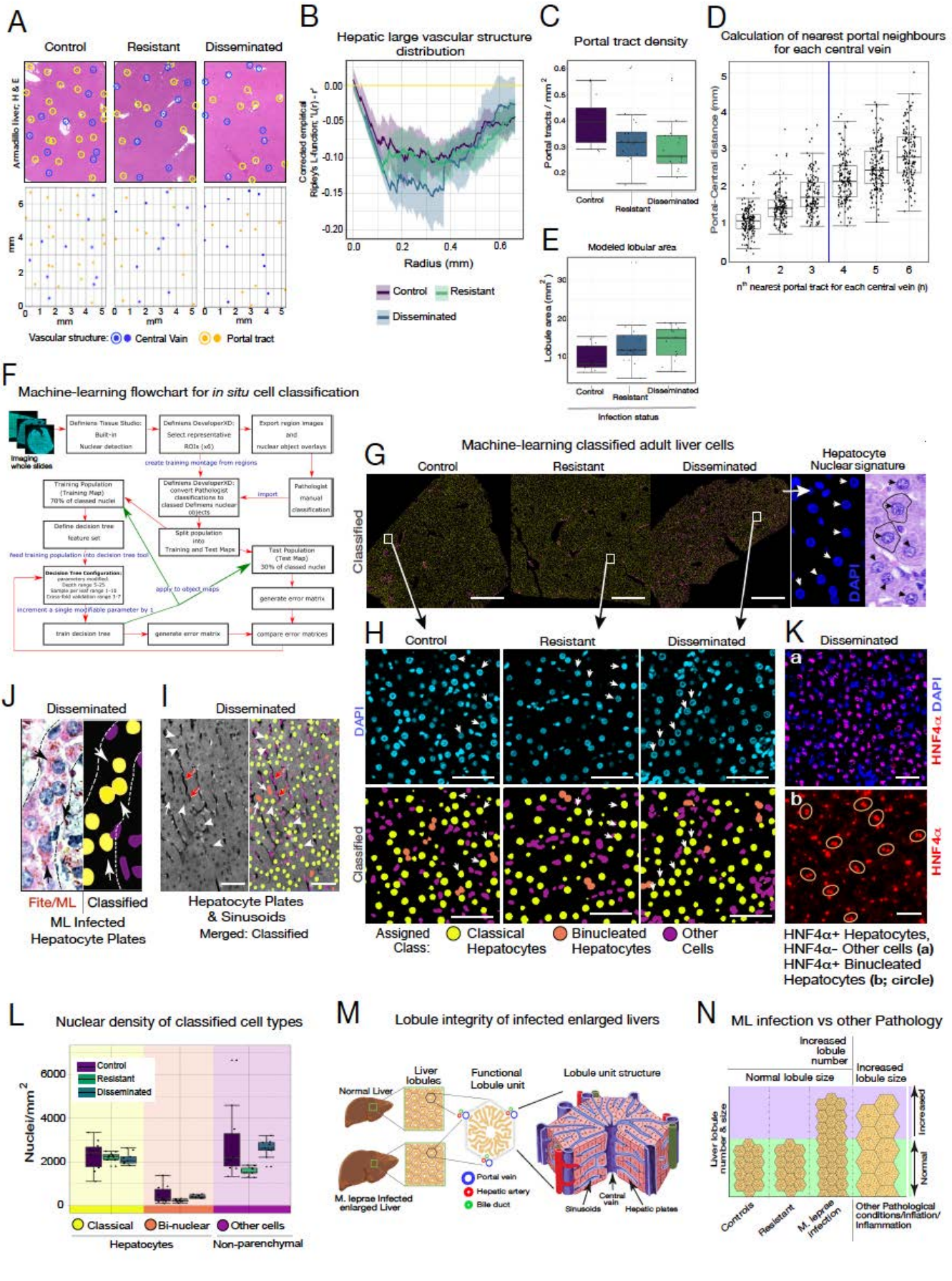

1387

Figure 3

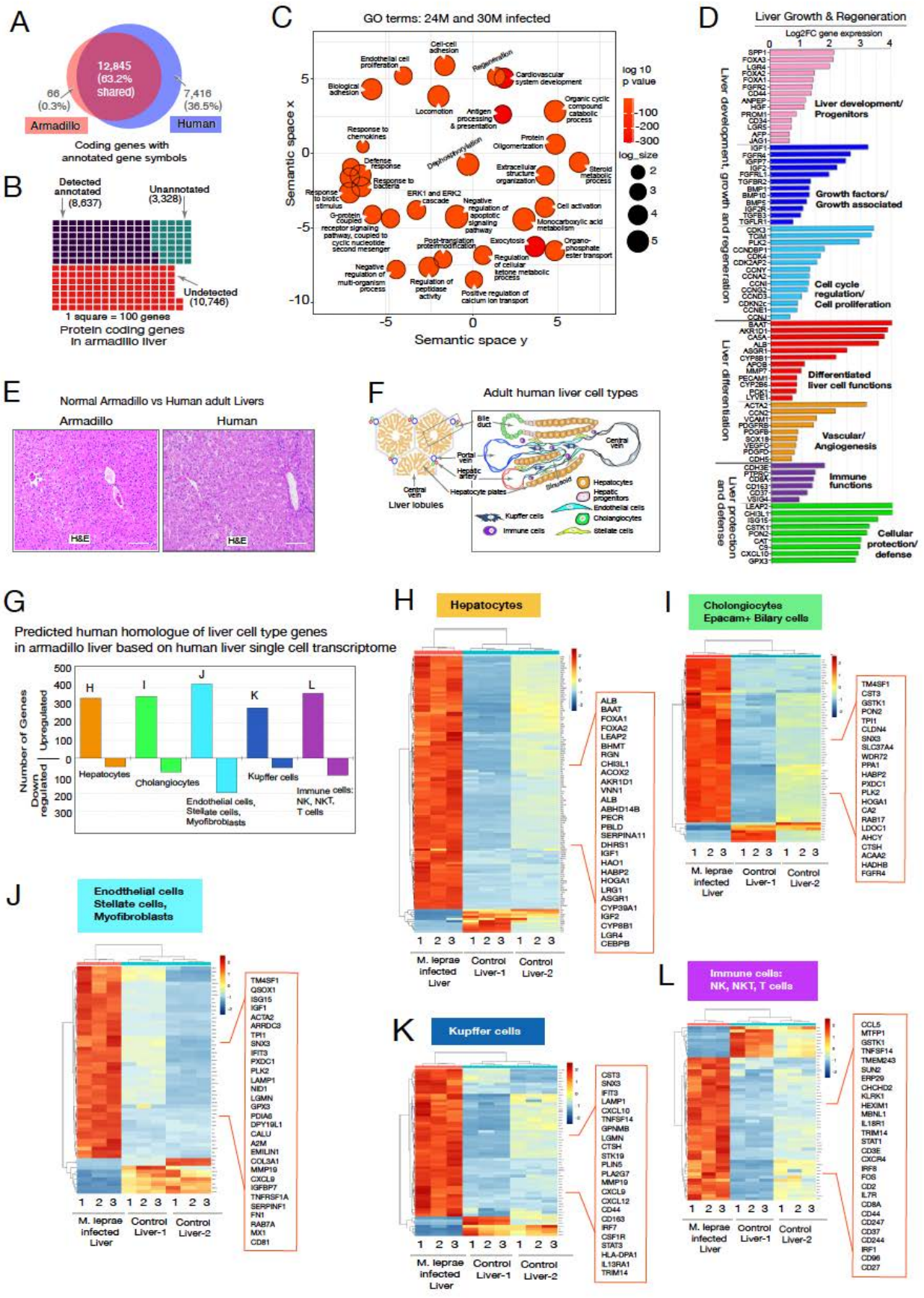
A
12,845 (63.2% shared)
66 (0.3%)
7,416 (36.5%)
Armadillo
Human
Coding genes with annotated gene symbols
B
Detected annotated (8,637)
Unannotated (3,328)
Undetected (10,746)
1 square = 100 genes
Protein coding genes in armadillo liver
C
GO terms: 24M and 30M infected
Semantic space x
Semantic space y
log 10 p value
log_size
D
Liver Growth & Regeneration
Log2FC gene expression
Liver development/ Progenitors
Growth factors/ Growth associated
Cell cycle regulation/ Cell proliferation
Differentiated liver cell functions
Vascular/ Angiogenesis
Immune functions
Cellular protection/ defense
Liver development, growth and regeneration
Liver differentiation
Liver protection and defense
E
Normal Armadillo vs Human adult Livers
Armadillo
Human
H&E
F
Adult human liver cell types
Liver lobules
Hepatocytes
Kupffer cells
Endothelial cells
Cholangiocytes
Stellate cells
Immune cells
G
Predicted human homologue of liver cell type genes in armadillo liver based on human liver single cell transcriptome
Number of Genes
Upregulated
Downregulated
Hepatocytes
Cholangiocytes
Endothelial cells, Stellate cells, Myofibroblasts
Kupffer cells
Immune cells: NK, NKT, T cells
H
Hepatocytes
I
Cholongiocytes Epcam+ Bilary cells
J
Enodthelial cells Stellate cells, Myofibroblasts
K
Kupffer cells
L
Immune cells: NK, NKT, T cells
M. leprae infected Liver
Control Liver-1
Control Liver-2

Figure 4

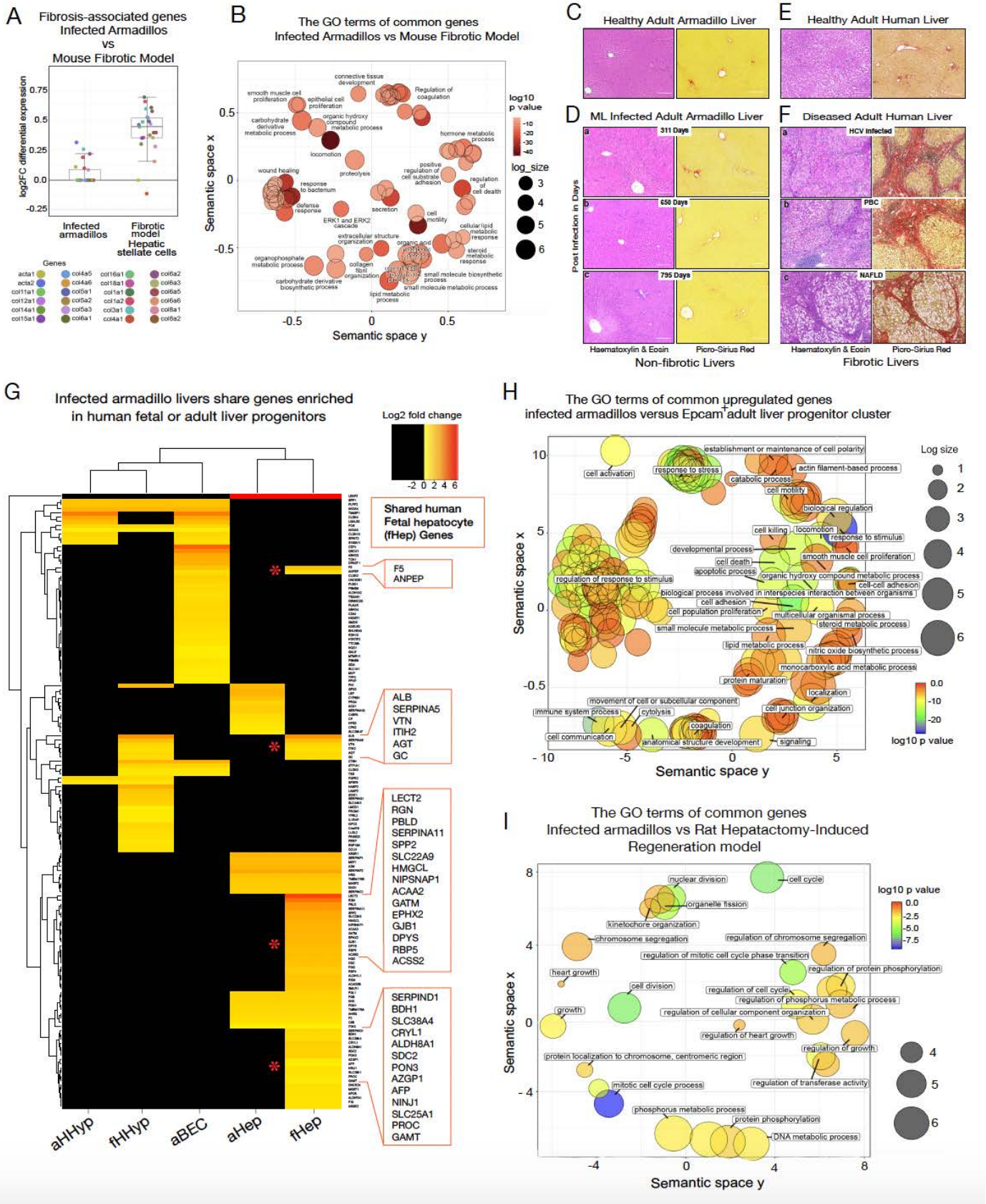
A
Fibrosis-associated genes
Infected Armadillos
vs
Mouse Fibrotic Model
log2FC differential expression
Infected armadillos
Fibrotic model Hepatic stellate cells
Genes
B
The GO terms of common genes
Infected Armadillos vs Mouse Fibrotic Model
Semantic space x
Semantic space y
log10 p value
log_size
C
Healthy Adult Armadillo Liver
E
Healthy Adult Human Liver
D
ML Infected Adult Armadillo Liver
311 Days
650 Days
795 Days
Post Infection in Days
Haematoxylin & Eosin
Picro-Sirius Red
Non-fibrotic Livers
F
Diseased Adult Human Liver
HCV Infected
PBC
NAFLD
Haematoxylin & Eosin
Picro-Sirius Red
Fibrotic Livers
G
Infected armadillo livers share genes enriched
in human fetal or adult liver progenitors
Log2 fold change
Shared human Fetal hepatocyte (fHep) Genes
F5
ANPEP
ALB
SERPINA5
VTN
ITIH2
AGT
GC
LECT2
RGN
PBLD
SERPINA11
SPP2
SLC22A9
HMGCL
NIPSNAP1
ACAA2
GATM
EPHX2
GJB1
DPYS
RBP5
ACSS2
SERPIND1
BDH1
SLC38A4
CRYL1
ALDH8A1
SDC2
PON3
AZGP1
AFP
NINJ1
SLC25A1
PROC
GAMT
aHHyp
fHHyp
aBEC
aHep
fHep
H
The GO terms of common upregulated genes
infected armadillos versus Epcam+ adult liver progenitor cluster
Log size
log10 p value
Semantic space x
Semantic space y
I
The GO terms of common genes
Infected armadillos vs Rat Hepatactomy-Induced
Regeneration model
log10 p value
Semantic space x
Semantic space y

Figure 5

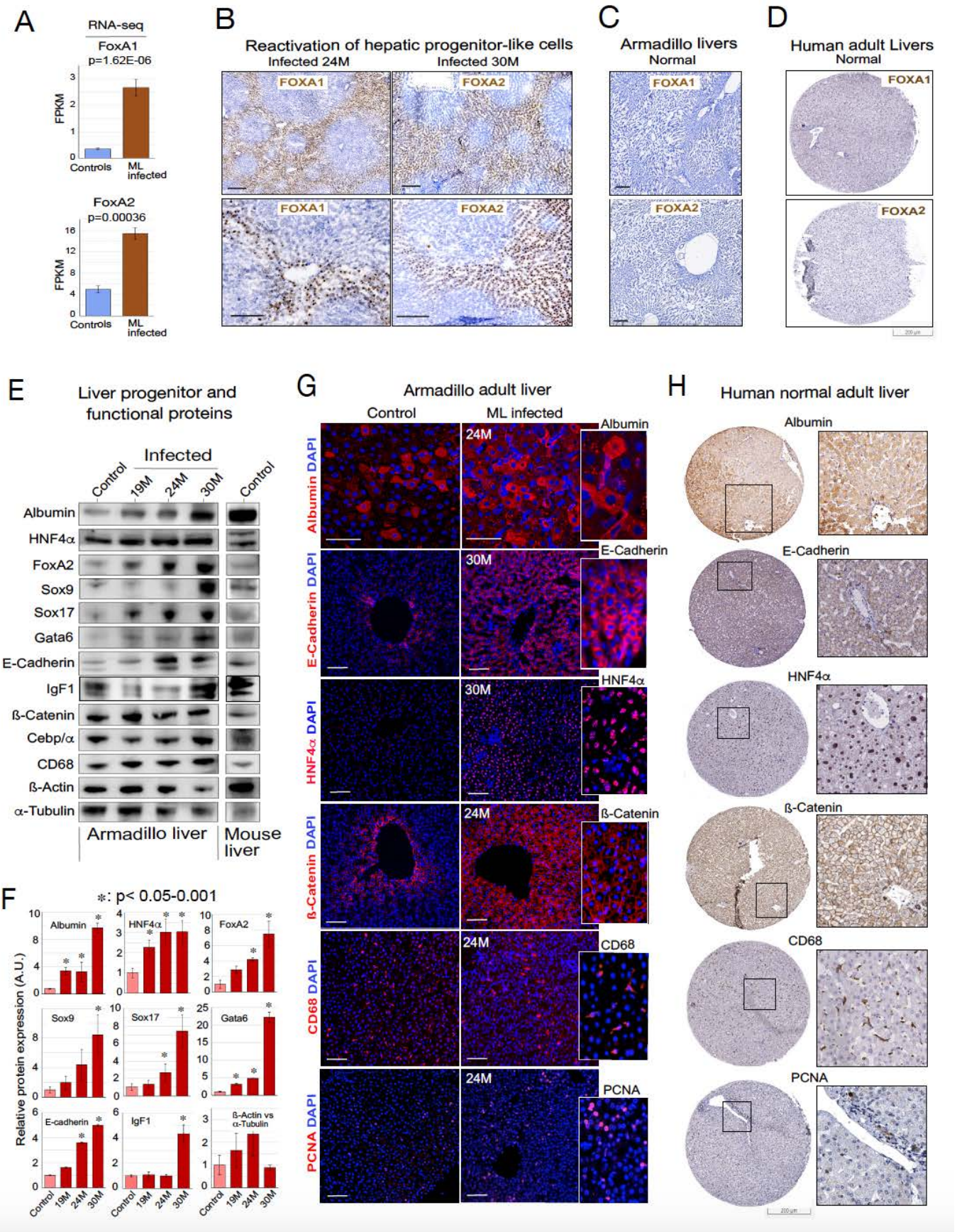

1390

Figure 6

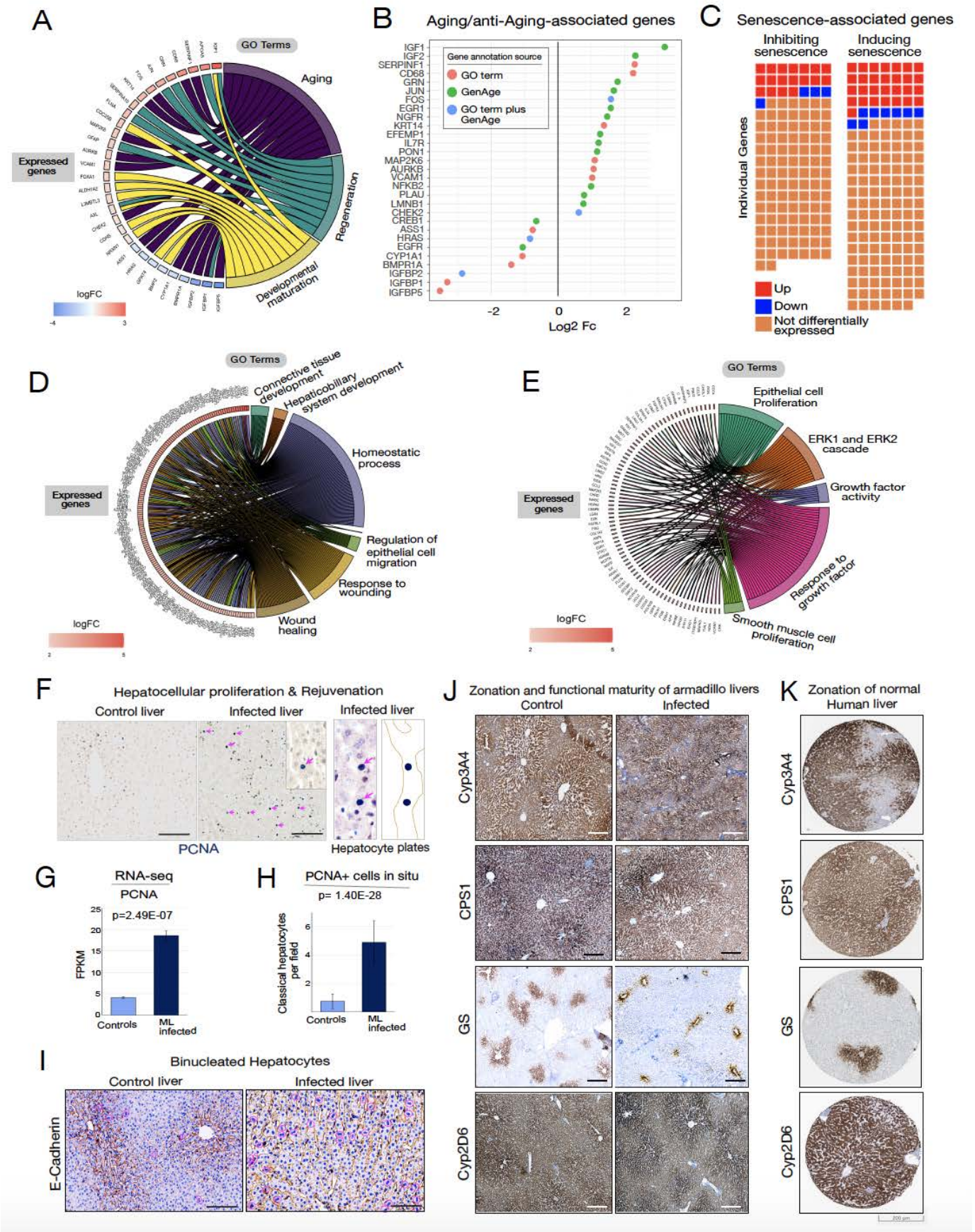

1391

Figure 7

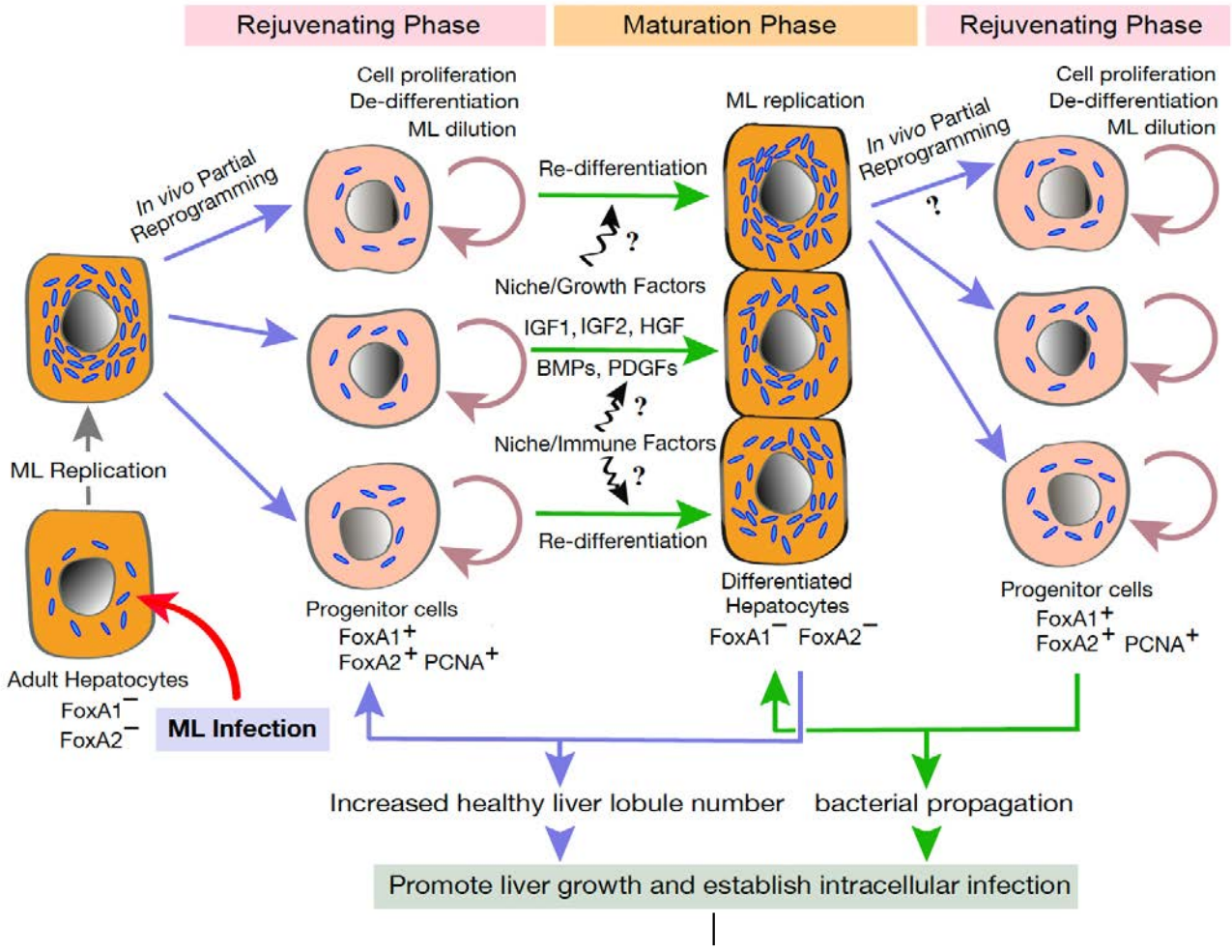

Functional *in vivo* liver organ growth with bacteria in living animals